

AD-A227 451

REF FILE COPY

4

Technical Report 1333
June 1990

Canonical Eigenvalues

Part II. Application to One-Layer,
Bounded, Underwater Acoustic
Ducts

Melvin A. Pedersen
David F. Gordon
Fell Hosmer

DTIC
ELECTE
OCT 04 1990
S E D

NAVAL OCEAN SYSTEMS CENTER

San Diego, California 92152-5000

J. D. FONTANA, CAPT, USN
Commander

R. M. HILLYER
Technical Director

ADMINISTRATIVE INFORMATION

This report was completed under funding from the Naval Ocean Systems Center Independent Research Program in an FY 89 project entitled "Canonical Eigenvalues in Acoustic Ducts." Melvin A. Pedersen contributed to this project as a private individual.

The need for a canonical approach to normal-mode eigenvalues became apparent and was initiated during earlier work. This earlier work was on acoustic propagation in double ducts and was sponsored jointly by ONR, Code 4250A, and the CNM Laboratory Participation Special Focus Program in FY 85 and 86.

Released by
E. F. Rynne, Jr., Head
Acoustic Analysis Branch

Under authority of
T. F. Ball, Head
Acoustic Systems and
Technology Division

CONTENTS

INTRODUCTION	1
SECTION 1. RESULTS FOR ONE-LAYER BOUNDED DUCTS	2
CANONICAL EIGENVALUES	2
CANONICAL FREQUENCY PLOTS	8
PHASE VELOCITY	10
GROUP VELOCITY	13
EIGENFUNCTION NORMALIZATION CONSTANTS	18
SECTION 2. SUMMARY	28
REFERENCES	30
APPENDIXES:	
A. Comparison of Phase Velocity for Case A and Case B	A-1
B. Duct Cutoff Frequencies	B-1
C. Limits of the Various Normalization Components	C-1

FIGURES

1. Schematic of one-layer duct with free surface and rigid bottom.	2
2. Canonical eigenvalues for the free-rigid boundaries.	3
3. Canonical eigenvalues for the free-free boundaries.	5
4. Canonical eigenvalues for the rigid-rigid boundaries.	6
5. Canonical frequency plot for the free-rigid boundaries.	9
6. Canonical frequency plot for the free-free boundaries.	9
7. Canonical frequency plot for the rigid-rigid boundaries.	9
8. Example of phase velocity vs frequency for the free-rigid boundaries.	11
9. Example of phase velocity vs frequency for the free-free boundaries.	11
10. Example of phase velocity vs frequency for the rigid-rigid boundaries.	11
11. Canonical group velocity factor for the free-rigid boundaries.	14
12. Canonical group velocity factor for the free-free boundaries.	14
13. Canonical group velocity factor for the rigid-rigid boundaries.	15
14. Example of group velocity vs frequency for the free-rigid boundaries.	15
15. Example of group velocity vs frequency for the free-free boundaries.	16
16. Example of group velocity vs frequency for the rigid-rigid boundaries.	16
17. Canonical normalization coefficient for the free-rigid boundaries.	20
18. Canonical normalization coefficient for the free-free boundaries.	20
19. Canonical normalization coefficient for the rigid-rigid boundaries.	21
20. Eigenvalue normalization coefficient for the free-rigid boundaries.	21
21. Eigenvalue normalization coefficient for the free-free boundaries.	22
22. Eigenvalue normalization coefficient for the rigid-rigid boundaries.	22
23. Counterpart of Fig. 17 for alternative normalization.	24

24. Counterpart of Fig. 18 for alternative normalization.	24
25. Counterpart of Fig. 19 for alternative normalization.	25
26. Counterpart of Fig. 20 for alternative normalization.	26
27. Counterpart of Fig. 21 for alternative normalization.	26
28. Counterpart of Fig. 22 for alternative normalization.	27

INTRODUCTION

Reference 1 presents the general theory of canonical eigenvalues. This report applies that theory to underwater sound propagation in a one-layer bounded duct. The canonical eigenvalue equation for a multilayered profile is a function of two dimensionless mathematical variables, x and y , and two sets of dimensionless parameters, ρ_i and S_i . The parameter ρ_i is a function of the ratio of sound-speed gradients at layer interfaces, while the parameter S_i involves ratios of three successive interface sound speeds. The canonical eigenvalues are curves of y vs x for a fixed set of ρ_i and S_i , which total $2(I-1)$ parameters for a bounded profile of I layers.

The eigenvalues are referred to as canonical because they do not apply to just one profile as in the customary approach. They apply for some given boundary condition to an entire class of profiles, viz., the subset of all I -layered profiles as constrained by the fixed set of ρ_i and S_i .

For a one-layered bounded profile, there are no ρ_i and S_i parameters to constrain the profiles. The set of curves of y vs x for a given boundary condition represents the canonical eigenvalues for the entire class of one-layer bounded profiles with the given boundary condition. This report deals with three pairs of boundary conditions. These are a free surface and rigid bottom, a free surface and free bottom, and a rigid surface and rigid bottom.

Section 1 presents numerical examples for canonical eigenvalues, phase velocity, group velocity, and eigenfunction normalization coefficients as well as for certain other auxiliary functions referred to as canonical frequency, canonical group velocity factor, and canonical normalization coefficient. In the computational process, these auxiliary functions are generated along with the canonical eigenvalues. These auxiliary functions, however, will not be presented until they arise in the orderly progression of results. Numerical examples for the three sets of boundary conditions are presented in parallel, because it is of interest to compare the three sets as the progression of results is presented. Although Section 1 is primarily concerned with numerical results, it deals with theoretical analysis as the need arises.

Section 2 presents a summary. Appendixes A, B, and C treat the more involved proofs of various characteristics of the canonical eigenvalues.

Version For	
CPA&I	<input checked="" type="checkbox"/>
NO TAB	<input type="checkbox"/>
Unreduced	<input type="checkbox"/>
Collection	
Distribution/	
Availability Codes	
Avail and/or	
Special	
A-1	

SECTION 1. RESULTS FOR ONE-LAYER BOUNDED DUCTS

The one-layer bounded ducts fall into three profile classes. The class of most interest in underwater acoustics is illustrated in Fig. 1. Here the surface boundary is free, while the bottom boundary is rigid. As with all canonical profile classes, the profiles are divided into two cases: Case A with a positive slope and Case B with a negative slope.

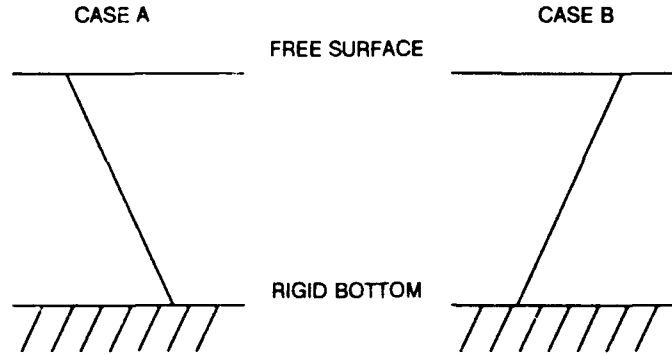


Figure 1. Schematic of one-layer duct with free surface and rigid bottom.

A second profile class is that of the free surface, free bottom. A third profile class is that of the rigid surface, rigid bottom. These two profile classes are primarily of interest only theoretically for underwater acoustics. They might, however, have practical application in other disciplines involving wave equation solutions. Our interest here is how these different boundary conditions affect the canonical eigenvalue solutions and subsequent results.

A fourth profile class—rigid surface and free bottom—presents nothing new, since the results are essentially the same as for the first class of Fig. 1. (If we turn class 4 upside down, we have class 1.)

We next define four functions of x and y :

$$G_1 = Ai(-x) Bi(-y) - Bi(-x) Ai(-y) \quad (1)$$

$$G_2 = Ai(-x) Bi'(-y) - Bi(-x) Ai'(-y) \quad (2)$$

$$G_3 = Ai'(-x) Bi(-y) - Bi'(-x) Ai(-y) \quad (3)$$

$$G_4 = Ai'(-x) Bi'(-y) - Bi'(-x) Ai'(-y) \quad (4)$$

Here x and y represent the Airy function argument evaluated at the surface and bottom, respectively. Most of the functions of x and y of interest in the canonical approach can be expressed in terms of these four functions.

CANONICAL EIGENVALUES

The eigenvalue equation for the duct of Fig. 1 is

$$G_2 = 0 \quad (5)$$

where G_2 is given by Eq. 2. Equation 5 guarantees that the F_1 of Eq. 2 of Ref. 1 vanishes at the surface boundary and that dF_1/dZ vanishes at the rigid bottom. Figure 2 presents the solutions of Eq. 5.

Observe the line $y = x$. As discussed in Eq. 15 and 16 of Ref. 1, this line separates the modes into two families. Those modes that lie below the line are associated with Case A of Fig. 1; the modes that lie above the line are associated with Case B. As we shall demonstrate later, the numbers associated with Case A or B for each eigenvalue curve are mode numbers, i.e., the mode count increases as each family member moves away from the line $y = x$.

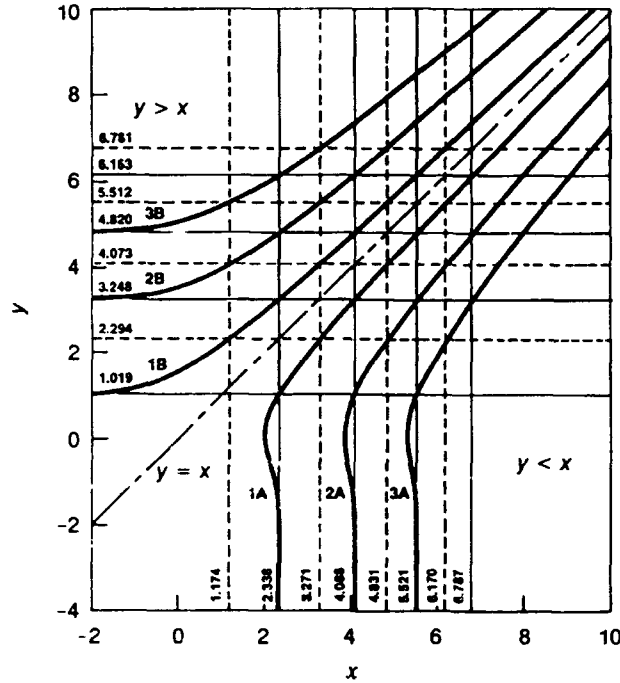


Figure 2. Canonical eigenvalues for the free-rigid boundaries.

Consider next the solid vertical and horizontal grid lines. The vertical lines are solutions or roots of

$$Ai(-x) = 0 \quad (6)$$

while the horizontal lines are solutions of

$$Ai'(-y) = 0 \quad (7)$$

The numerical value of these roots are marked on the grid lines. One may readily verify that the x, y combinations of Eq. 6 and 7 satisfy Eq. 5. Thus, the intersections of the grid lines represent lattice points, which the eigenvalue curves must pass through. In addition to the finite zeros, Eq. 6 and 7 go to zero asymptotically for large negative values of x and y , respectively. The lattice points at $x = -\infty$ are manifest in Fig. 2 by the horizontal asymptotes at the zeros of Eq. 7 for the Case B curves. The lattice points at $y = -\infty$ are manifest in Fig. 2 by the vertical asymptotes at the zeros of Eq. 6 for the Case A curves.

Now consider the dashed vertical and horizontal grid lines. The vertical lines are solutions of

$$Bi(-x) = 0 \quad (8)$$

while the horizontal lines are solutions of

$$Bi'(-y) = 0 \quad (9)$$

These lines are also labeled with the numerical value of the roots. These x, y combinations again satisfy Eq. 5 and represent lattice points, which the eigenvalue curves must pass through. Equations 8 and 9 have only finite zeros. Thus, there are no asymptotes associated with the dashed grid lines.

One can readily predict the curves by connecting the lattice points and noting that each lattice point must lie on one curve. The only areas which really need a detailed solution of Eq. 5 are the case A curves for $y < 1.019$ and the case B curves for $x < 1.174$.

The curves of Fig. 2 were generated by solving Eq. 5 by iteration with Newton's method. Two approaches were used. The first approach was to select a y and iterate on x to find the x solution for the fixed y . This approach makes use of

$$\delta G_2 / \delta x = -G_4 \quad (10)$$

The second approach was to select an x and iterate on y to find the y solution for the fixed x . This approach makes use of

$$\delta G_2 / \delta y = y G_1 \quad (11)$$

Our approach is a "mode follower routine" which traces out a continuous x, y curve corresponding to some mode. We start the iterative process near a lattice point, where we have good estimates of the solution, and trace the curve by moving first to lower values of x and y and then to higher values of x and y . First estimates for each iteration are obtained by extrapolating the known solution. Once the first curve has been traced, we can trace a second curve, starting at any lattice point that does not lie on the first curve. Additional curves are traced by starting at any lattice point that does not lie on curves already traced.

The approach of Eq. 11 works best for the Case B curves; that of Eq. 10 works best for the Case A curves. Equation 10 can run into trouble for Case B curves, because the tracing process may select a y for which the curve does not exist. Equation 11 can run into trouble for Case A curves, because the tracing process may select an x for which the curve does not exist. Moreover, Eq. 11 vanishes at $y = 0$, as evidenced by the vertical slopes for the Case A curves at this point. This causes the routine to fail if one attempts to use Eq. 11 in the region near $y = 0$.

We have already associated the two families of modes with Case A and Case B of Fig. 1 on the basis of their relation to the line $y = x$. There is a second mathematical property which confirms this association. Observe that the B family of modes all cross $x = 0$, but not $y = 0$. From Eq. 17 of Ref. 1, $C_p = C_1$ when $x = 0$. This corresponds to a ray which grazes the ocean surface and can only occur for Case B in Fig. 1. Similarly, the A family of modes all cross $y = 0$, but not $x = 0$. From Eq. 8 of Ref. 1, we can establish that $C_p = C_2$ when $y = 0$. This corresponds to a ray, which grazes the ocean bottom, and can only occur for Case A in Fig. 1.

We next address the free-surface, free-bottom profile. Figure 3 is the counterpart of Fig. 2, and the counterparts of Eq. 5 to 11 are, respectively

$$G_1 = 0 \quad (12)$$

$$Ai(-x) = 0 \quad (13)$$

$$Ai(-y) = 0 \quad (14)$$

$$Bi(-x) = 0 \quad (15)$$

$$Bi(-y) = 0 \quad (16)$$

$$\delta G_1 / \delta x = -G_3 \quad (17)$$

and

$$\delta G_1 / \delta y = -G_2 \quad (18)$$

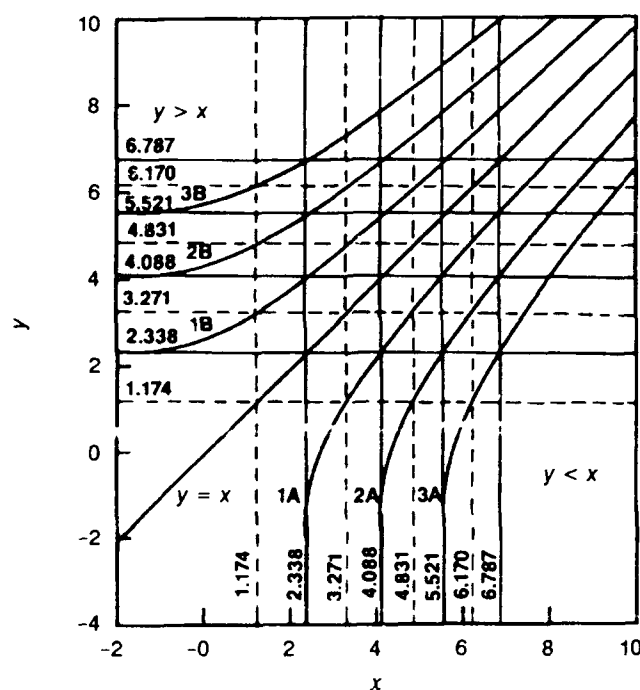


Figure 3. Canonical eigenvalues for the free-free boundaries.

Figure 2 has many features similar to Fig. 1. There are, however, two important differences. The first difference is that $y = x$ is a solution to Eq. 12. This is readily verified from Eq. 1. Observe also that the line goes through a set of lattice points. The line $y = x$ represents a degenerate mathematical solution which is discarded physically because it corresponds to zero frequency for all values of $y = x$. A second difference is that the two families of modes are symmetric about the line $y = x$. This may be demonstrated by noting that Eq. 12 is unchanged when x and y are interchanged. What this means physically is that Case B may be considered to be Case A turned upside down.

We now address the rigid-surface, rigid-bottom profile. Figure 4 is the counterpart of Fig. 2, and the counterparts of Eq. 5 to 11 are, respectively

$$G_4 = 0 \quad (19)$$

$$Ai'(-x) = 0 \quad (20)$$

$$Ai'(-y) = 0 \quad (21)$$

$$Bi'(-x) = 0 \quad (22)$$

$$Bi'(-y) = 0 \quad (23)$$

$$\delta G_4 / \delta x = x G_2 \quad (24)$$

and

$$\delta G_4 / \delta y = y G_3 \quad (25)$$

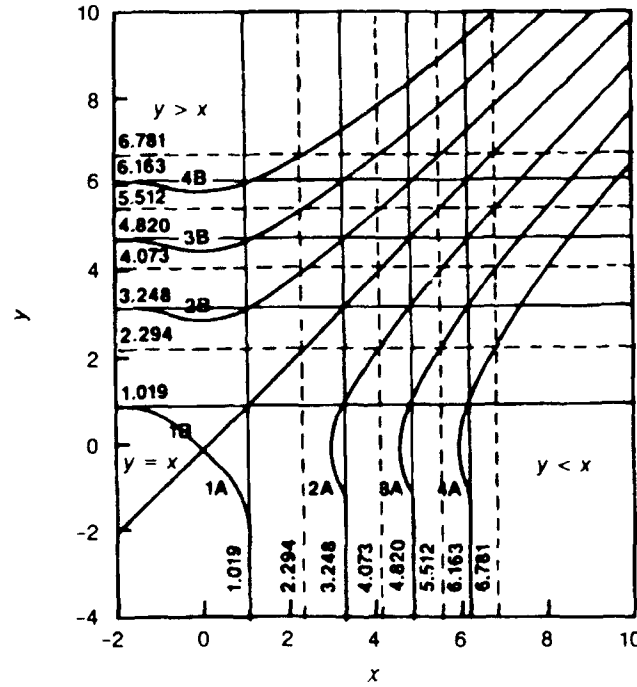


Figure 4. Canonical eigenvalues for the rigid-rigid boundaries.

Figure 4 is similar to Fig. 3 in that the line $y = x$ is a solution and the two families of modes are symmetric about the line $y = x$. The real surprise is the strange behavior of mode 1. Our first impression was that the results for mode 1 were in error. However, as discussed later, this curve is compatible with the result that mode 1 for a duct with rigid boundaries can never correspond to reflection from both boundaries. In Fig. 4, the mode 1 curves meet at $x = 0, y = 0$. Mode 1A never crosses into positive y . Thus, the mode corresponds to a ray which never reflects from the bottom interface. Similarly, Mode 1B never crosses into positive x . Thus, the mode corresponds to a ray which never reflects from the surface interface.

The nature of the mode 1 curve can be inferred from the characteristics of the lattice points. There must be a 1B curve which is asymptotic to $y = 1.019$ and a 1A curve which is asymptotic to

$x = 1.019$ because of the zeros of Ai' at x or $y = -\infty$. However, the 1B and 1A curves cannot cross into $y > 1.019$ or $x > 1.019$ because all of the lattice points in this region already lie either on one of the curves for higher-order modes or on the line $y = x$.

We will need to know the nature of the solution for 1A and 1B as the origin is approached. Observe in Fig. 4 that the eigenvalue curve appears to cross the curve $y = x$ at right angles. This suggests that the line

$$y = -x \quad (26)$$

is an approximate solution to Eq. 19 for mode 1. If we assume that Eq. 26 holds, G_4 of Eq. 4 becomes

$$G_4(x, -x) = Ai'(-x) - Bi'(-x) Ai'(x) \quad (27)$$

We next evaluate Eq. 27 by means of the series expansions given in Sections 10.4.2 to 10.4.5 of Ref. 2. After much manipulation and simplification, we obtain

$$G_4(x, -x) = (8/15)3^{1/2} C_1 C_2 x^5 \quad (28)$$

where C_1 and C_2 are constants given in Ref. 2. The numerical value of the coefficient of x^5 in Eq. 28 is 0.0848826. The results of Eq. 27 were compared with those of Eq. 28 for $x = 0.5$. The value of Eq. 28 was 0.0026526 and agreed with Eq. 27, with a difference of 1 in the fifth significant digit. Since the error in the approximate solution of Eq. 26 varies as x^5 , it is accurate near the origin. Indeed, Fig. 4 shows little departure from Eq. 26 until $|x| > 0.5$. Equation 26 will be useful in the analysis of phase velocity for modes 1A and 1B.

There is another feature of interest in Fig. 2 to 4. Consider the spacing between modes at larger values of x and y , away from the vertical and horizontal asymptotes. In Fig. 2, the spacing is about the same between modes 1A and 1B as it is between adjacent modes of family A and family B. Similarly, in Fig. 3 and 4, the spacing between the line $y = x$ and mode 1A or mode 1B is about the same as it is between adjacent modes of family A and family B. This near-regular spacing between mathematical solutions is a property of solutions to eigenvalue equations.

Our contention is that the eigenvalue solutions in mathematical space are more predictable and provide more information than in customary physical space. For example, the mathematic solutions for both mode families and the $y = x$ solutions all fit into a consistent pattern. In contrast, the customary solutions in physical space for family A have no apparent connection with the solutions for family B, and there is no counterpart at all for the solutions given by $y = x$.

Our plans call for a systematic investigation of canonical eigenvalue plots for two and even more layers. We believe that these plots will display a behavior which fits into a regular scheme that is more predictable than the customary plots in physical space.

CANONICAL FREQUENCY PLOTS

Canonical frequency plots apply to the entire class of profiles. The frequency for a specific profile of the class is given by Eq. 14 of Ref. 1 and may be obtained by multiplying the canonical frequency by a scale factor which depends on the profile parameters.

Figures 5 to 7 are the respective canonical frequency plot counterparts of Fig. 2 to 4. These are obtained by evaluating $|y - x|^{3/2}$ from the eigenvalue curves of Fig. 2 to 4 and plotting the result vs x . Mode family A is given by the solid curves and mode family B by the dashed curves. These curves apply to all profiles of the class.

Before discussing the properties of the curves, we demonstrate how to obtain the acoustic frequency for some particular desired profile of the class. We shall use the same sound-speed profiles throughout this report when we need to evaluate quantities that are dependent on a specific profile. The example profile chosen for Case A is $C_1 = 1480$ m/s, $C_2 = 1482$ m/s, and $\gamma_1 = 0.02\text{s}^{-1}$. The example profile chosen for Case B is $C_1 = 1482$ m/s, $C_2 = 1480$ m/s, and $\gamma_1 = -0.02\text{s}^{-1}$. These profiles are selected to be quite similar in that the maximum and minimum sound speeds are the same and the surface gradient has the same magnitude. The layer thickness is 99.80 m for Case A and 100.20 m for Case B. The frequency scale factor of Eq. 14 of Ref. 1 is 45.44 for Case A and 45.26 for Case B. Thus, for example, the frequency corresponding to an ordinate of 4.0 in Fig. 5 to 7 is about 182 Hz for the given profiles.

Consider now the properties of the canonical frequency curves. As x approaches ∞ , the frequency for both families and for all three boundary conditions goes to zero asymptotically. A proof is given in Appendix B, where it is demonstrated that $y - x$ goes to zero for all modes. What happens is that all of the eigenvalue curves of Fig. 2 to 4 approach the line $y = x$ asymptotically for large values of x . An exception is mode 1 of Fig. 4 and 7. Here, f goes to zero for mode 1A as x approaches zero from positive values, and f goes to zero for mode 1B as x approaches zero from negative values. This zero limit on f follows immediately from Eq. 14 of Ref. 1 and Eq. 26.

The canonical frequency plots always have vertical asymptotes for the A family of modes at the same values of x as the vertical asymptotes of the corresponding Fig. 2 to 4. From Eq. 14 of Ref. 1, we see that infinite negative y and fixed x leads to infinite f . For the Case B family, there are no vertical asymptotes. However, from Eq. 14 of Ref. 1, it is clear that f goes to infinity for large negative x for the B family of modes. Here, y is fixed as x goes to minus ∞ . The important feature here is that f goes to infinity for either $x \rightarrow -\infty$ or $y \rightarrow -\infty$. Whether the curves form vertical asymptotes or not is not important. For example if we had chosen y rather than x as the independent variable, we would find that the B family formed vertical asymptotes while the A family did not.

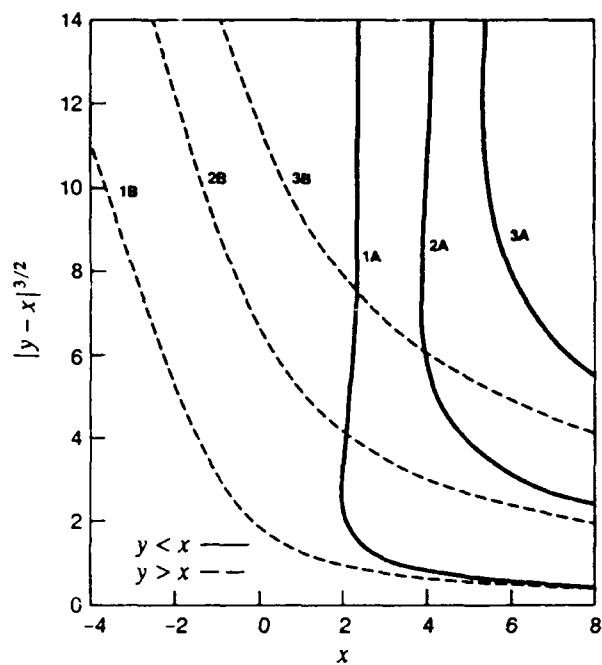


Figure 5. Canonical frequency plot for the free-rigid boundaries.

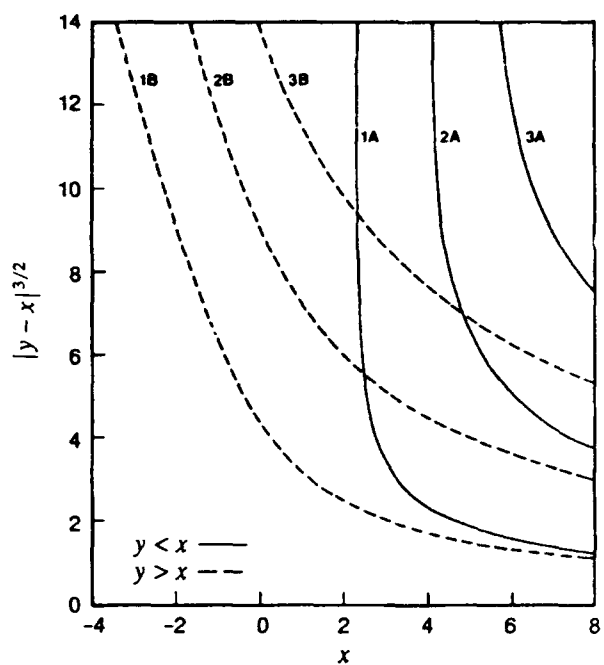


Figure 6. Canonical frequency plot for the free-free boundaries.

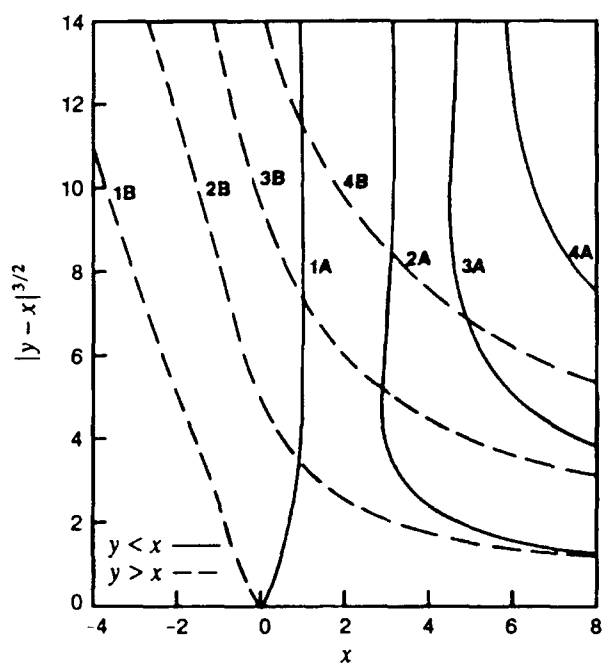


Figure 7. Canonical frequency plot for the rigid-rigid boundaries.

PHASE VELOCITY

Figures 8 to 10 are the phase velocity counterparts of Fig. 2 to 4, respectively. These curves were generated by Eq. 17 of Ref. 1 by using the values of f from Eq. 14 of Ref. 1, the canonical eigenvalue x , and the specified values of C_1 and γ_1 . Again, family A values are given as solid curves and family B values as dashed curves.

We note that the A and B curves are well separated in Fig. 8. However, in Fig. 9 and 10 the curves appear to be superimposed. Appendix A demonstrates that if the phase velocity is C_p for frequency f for Case A, then the same phase velocity occurs for frequency \bar{f} for Case B, where

$$\bar{f} = f(C_1/C_2)^3 \quad (29)$$

Here, C_1 and C_2 are the parameters for Case A. For the parameters of our sample profile, $(C_1/C_2)^3 = 0.9960$. Thus, the curves for Case B lie very slightly to the left of those for Case A.

The condition of Eq. 29 depends on the symmetry of the curves of Fig. 3 and 4 about the line $y = x$ and also in our choice of profile parameters for Case A and Case B. When we chose the parameters so that the Case A and Case B profiles would resemble each other, we had no idea that the phase velocity solutions would be almost identical for the boundary conditions of Fig. 3 and 4.

Although we determined phase velocity from Eq. 17 of Ref. 1, the following alternative expression is useful for demonstrating various features of the solution:

$$C_p = C_2 [1 - f^{2/3} \pi^{2/3} |\gamma_{10}|^{2/3} y]^{-1/2} \quad (30)$$

Equation 30 is obtained by solving Eq. 8 of Ref. 1 for C_p with $i = 1$. Both Eq. 17 of Ref. 1 and Eq. 30 hold. This follows because Eq. 14 of Ref. 1 provides the condition that they both hold. Indeed, Eq. 14 of Ref. 1 is most easily obtained by setting Eq. 17 of Ref. 1 and Eq. 30 equal and solving for f .

Equation 30 makes it apparent that $y = 0$ corresponds to $C_p = C_2$, as was previously mentioned in the discussion of Fig. 2. We chose to consider x as the independent and y as the dependent variable of the eigenvalue equation. However, we could have considered y as the independent variable and used Eq. 30 to determine C_p rather than Eq. 17 of Ref. 1.

Consider now the characteristics of the curves of Fig. 8 to 10 at the higher frequencies. From Eq. 17 of Ref. 1, it is clear that C_p goes to C_1 for the A family of modes, since x is a finite constant. Similarly, Eq. 30 demonstrates that C_p goes to C_2 for the B family of modes, since y is a finite constant. In Fig. 8 to 10, at high frequencies, C_p goes to 1480 m/s for both families of modes, because this is the minimum of the two boundary sound speeds chosen for our sample profiles.

Observe in Fig. 8 to 10 that the phase velocity becomes large at low frequencies. Indeed, the phase velocity goes to infinity for specific values of frequency. These frequencies are the cutoff frequencies for the duct. At lower frequencies, the phase velocity turns pure imaginary. These cutoff frequencies are best expressed in terms of wavelength as given by

$$f = N_0 C_1 Z_2^{-1} \quad (31)$$

where N_0 is the number of vertical wavelengths in the duct, C_1 is the surface sound speed, and Z_2 is the duct thickness.

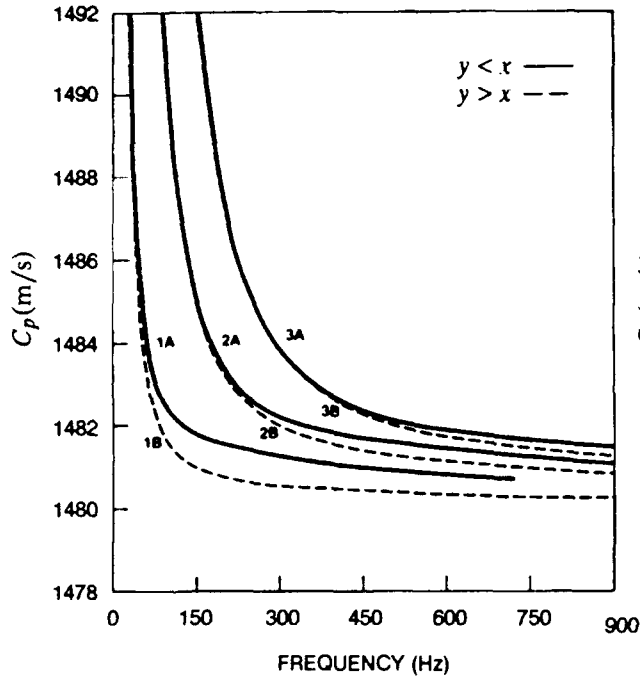


Figure 8. Example of phase velocity vs frequency for the free-rigid boundaries.

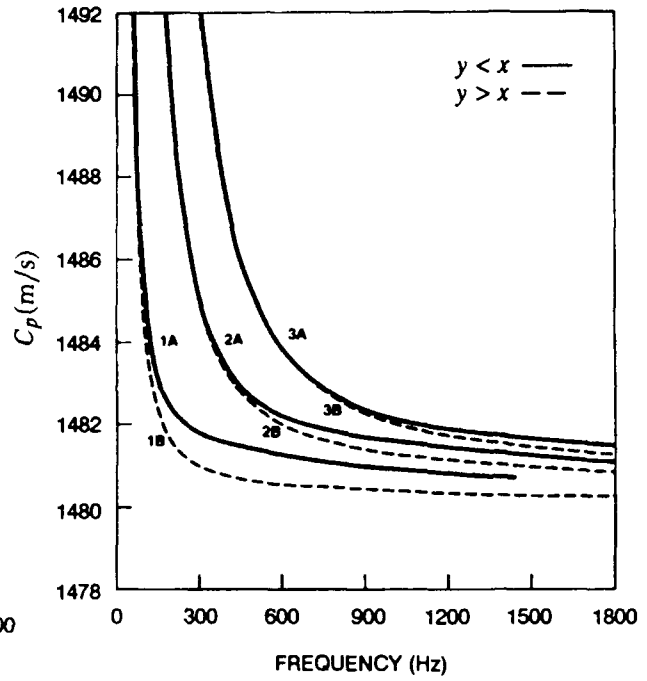


Figure 9. Example of phase velocity vs frequency for the free-free boundaries.

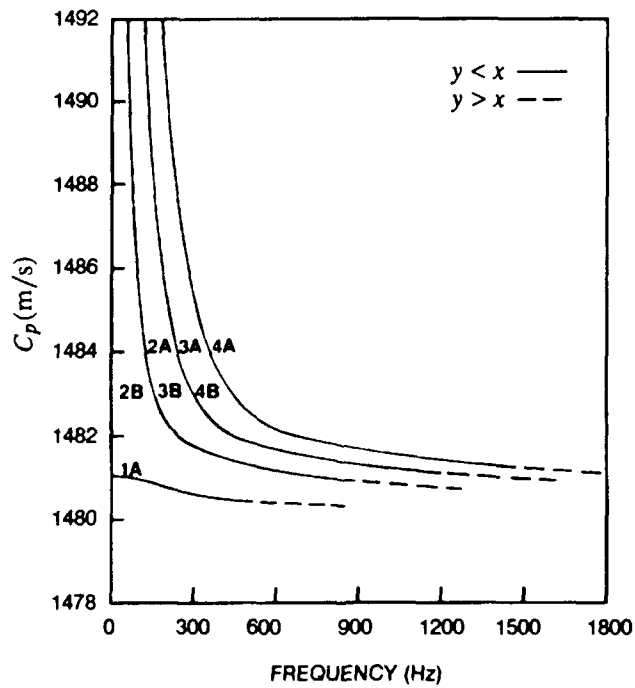


Figure 10. Example of phase velocity vs frequency for the rigid-rigid boundaries.

The number of wavelengths at cutoff for the free-rigid boundary condition is given by

$$N_0 = (2n - 1)/4 \quad (32)$$

where n is the mode number. The corresponding expression for the free-free and rigid-rigid boundary conditions are, respectively

$$N_0 = n/2 \quad (33)$$

and

$$N_0 = (n - 1)/2 \quad (34)$$

A rigorous derivation of Eq. 31 to 34 is given in Appendix B. The derivation is laborious and involves asymptotic representations of the x , y lattice points and several applications of the binomial expansion. However, the results can be explained rather simply in terms of the trigonometric functions, which represent good approximations to the Airy functions for these arguments. In Eq. 32, the standing wave is like a sine function, with a node at the surface and an antinode at the bottom. Here, mode n has n antinodes and n nodes. The antinodes at the bottom occur at odd multiples of a quarter wavelength.

In Eq. 33, the standing wave is like a sine function with nodes at the surface and bottom. Here, mode n has n antinodes and $n + 1$ nodes. The nodes at the bottom occur at multiples of one-half wavelength. In Eq. 34, the standing wave is like a cosine function, with antinodes at the surface and bottom. Here, mode n has n antinodes and $n - 1$ nodes. The antinodes at the bottom occur at multiples of one-half wavelength.

We note that for the sample profile parameters

$$C_1/Z_2 = 14.83 \text{ or } 14.79s^{-1} \quad (35)$$

or Case A or Case B, respectively. Thus, the cutoff frequencies for Case A or B are at odd multiples of 3.71 or 3.70 Hz, respectively, in Fig. 8 and are at all multiples of 7.42 or 7.40 Hz in Fig. 9 and 10.

On our first exposure to the cutoff frequencies, the result appeared at odds with a fundamental property for Sturm-Liouville equations, as discussed in Ref. 3. For our boundary conditions, the Sturm-Liouville eigenvalues, λ , are real; whereas our eigenvalues, C_p , turn imaginary below cutoff. However, $\lambda = \omega^2/C_p^2$. Thus, since our values of C_p are not complex but pure imaginary below cutoff, there is no contradiction. The eigenvalue λ is positive for frequencies above cutoff and negative for frequencies below cutoff.

We turn now to a discussion of mode 1 for the rigid-rigid boundary. There is no mode 1 for surface-reflected rays. This was pointed out in the discussion of Fig. 4 and is in agreement with the results of the phase-integral method as discussed in Ref. 4. For mode 1, Eq. 40 of Ref. 4 is zero and the phase-integral method has no solution. Also in Ref. 4, the phase-integral solution for mode n of the free-free boundary is the same as for mode $n - 1$ of the rigid-rigid boundary. We may determine from Fig. 3 and 4 that this is a very good approximation. The lattice points for n in Fig. 3 are similar to those for mode $n + 1$ in Fig. 4. This is true because the zeros of Ai lie close to those of Bi' and the zeros of Bi lie close to those of Ai' .

For an isovelocity duct, there is no mode 1 for the rigid-rigid boundary condition. However, for the profile of Eq. 1 of Ref. 1 with a sound-speed gradient, there is a mode 1 solution for refracted

rays, which reflect from only one boundary. The phase-integral method gives an approximate solution for $n = 1$ in Eq. 39 of Ref. 4. We next examine the behavior of phase velocity for mode 1 as x goes to zero. Equation 26 holds here, and the f of Eq. 14 of Ref. 1 goes to zero. The substitution of Eq. 26 into Eq. 14 of Ref. 1 and hence into Eq. 17 of Ref. 1 leads to

$$C_p = [(C_1^{-2} + C_2^{-2})/2]^{-1/2} \quad (36)$$

In other words, the square of the phase velocity corresponding to $f = 0$ for mode 1 of the rigid-rigid boundary condition is the harmonic mean of the square of the two boundary sound speeds.

In Fig. 10, the phase velocity for $f = 0$ appears to be 1481—midway between the boundary sound speeds. If we let

$$C_2 = C_1 + \Delta \quad (37)$$

we may expand Eq. 36 as a series in Δ to yield

$$C_p \cong C_1 + \Delta/2 - 3\Delta^2/8C_1 \quad (38)$$

The value of the first two terms of Eq. 38 is midway between C_1 and C_2 . For the sample profiles, the third term of Eq. 38 reduces C_p from the midpoint value to 1480.9990 m/s.

We note that Eq. 34 gives the correct result for $n = 1$ in that the cutoff frequency for mode 1 is zero. However, this result appears fortuitous because Eq. 34 represents the frequencies where the phase velocity is infinite, while f equals zero results in the finite value of Eq. 36. Not only is there no mode 1 for surface-reflected rays; there is no mode 1 for refracted rays with phase velocities between Eq. 36 and the larger of the sound speeds at the two boundaries.

GROUP VELOCITY

Figures 11 to 13 present the canonical group velocity factor L of Eq. 67 of Ref. 1, corresponding, respectively, to the eigenvalue curves of Fig. 2 to 4. The discussion of Fig. 11 to 13 is best included as part of the discussion of the group-velocity-vs-frequency curves, which are shown in Fig. 14 to 16, respectively.

These curves are generated from Eq. 69 of Ref. 1, which is interesting in that the frequency is not contained explicitly, but is implicitly in C_p and L . The procedure is to evaluate L and f from the eigenvalue curves, then evaluate C_p for that frequency, and then evaluate C_g for the C_p and L that corresponds to the frequency.

As was the case with the phase velocity, the group-velocity curves of Case A and Case B are almost superimposed in Fig. 15 and 16. With the use of Eq. 63 of Ref. 1 and Eq. 29, we can readily show that the group velocity is the same function of phase velocity for Case A as for Case B. This property can also be demonstrated from Eq. 69 of Ref. 1, but involves a tangle of involved algebraic manipulation which incredibly simplifies to the result obtained from Eq. 63 of Ref. 1 and Eq. 29. The net result is similar to that for the phase velocity. If the group velocity is C_g for frequency f for Case A, the same group velocity occurs for frequency \bar{f} for Case B, where \bar{f} is given by Eq. 29. Again, the group-velocity curves for Case B lie very slightly to the left of those for Case A.

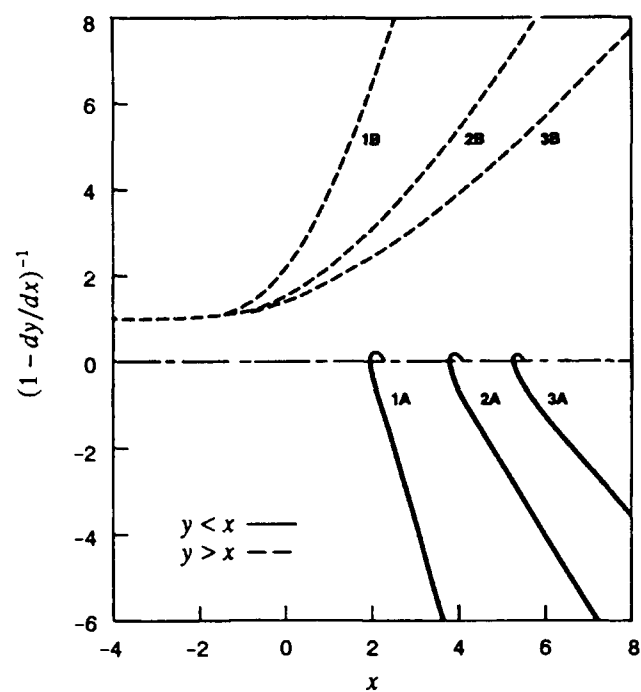


Figure 11. Canonical group velocity factor for the free-rigid boundaries.

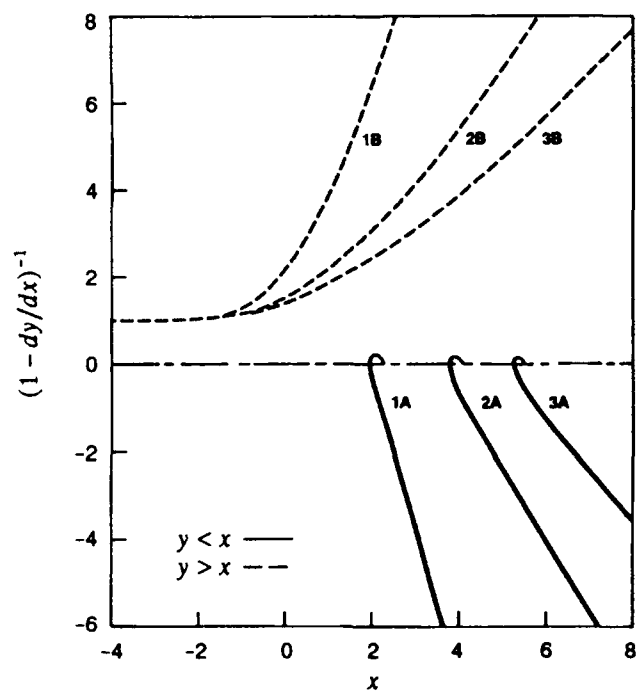


Figure 12. Canonical group velocity factor for the free-free boundaries.

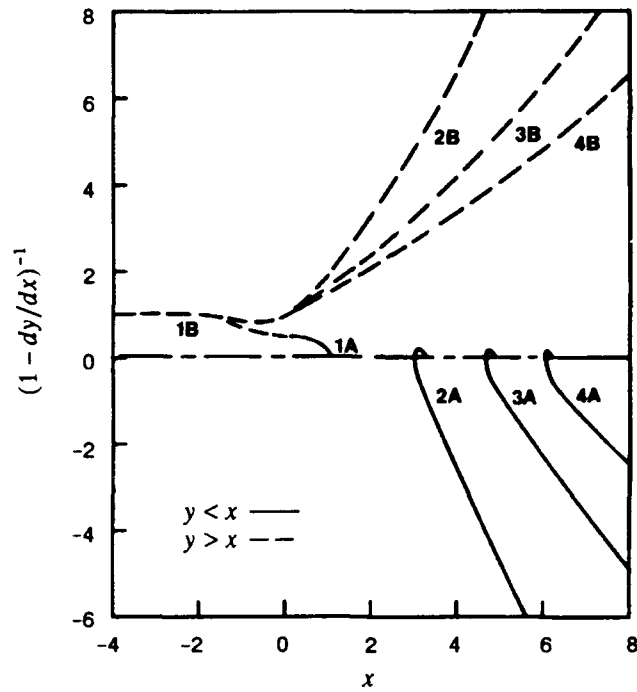


Figure 13. Canonical group velocity factor for the rigid-rigid boundaries.

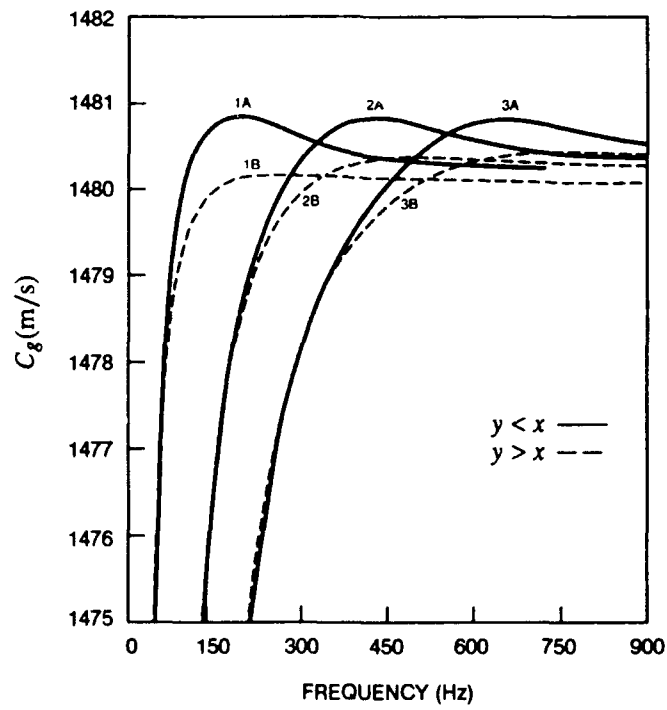


Figure 14. Example of group velocity vs frequency for the free-rigid boundaries.

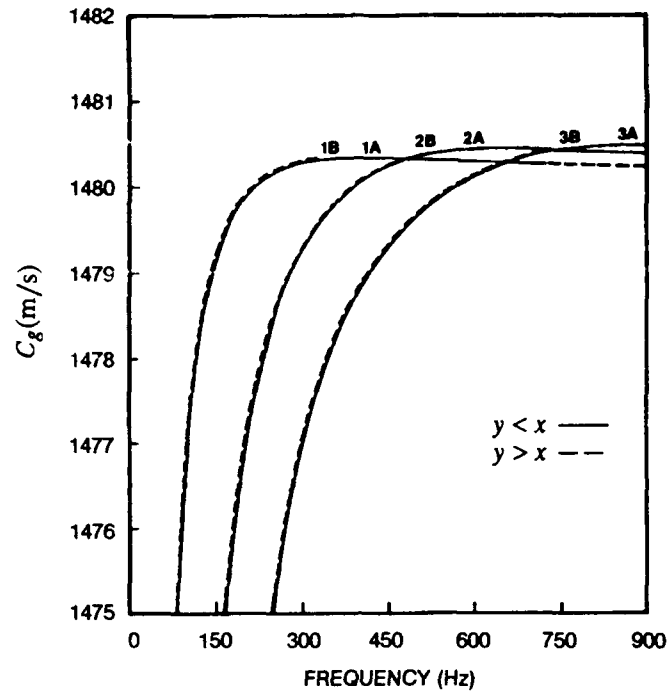


Figure 15. Example of group velocity vs frequency for the free-free boundaries.

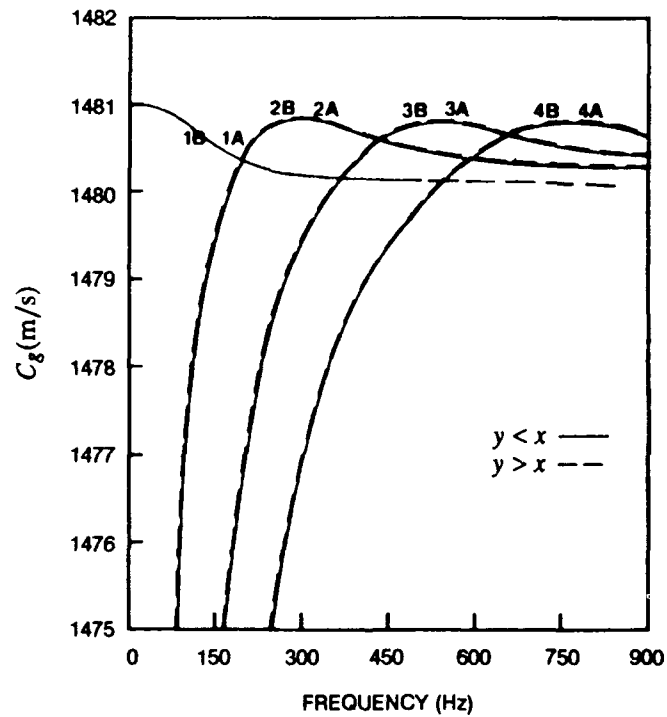


Figure 16. Example of group velocity vs frequency for the rigid-rigid boundaries.

It seems somewhat incredible that Eq. 69 of Ref. 1 can transform the obscure mathematical curves of Fig. 11 to 13 into the familiar physical curves of Fig. 14 to 16. However, we next provide a physical interpretation of Eq. 69 of Ref. 1. We consider first the Case A configuration. As indicated in the previous discussion of Eq. 69 and 70 of Ref. 1, the solution for the unbounded ducts of Ref. 4 is Eq. 69, with the third term in the brackets suppressed. This third term may then be considered as a correction term to the group velocity as given by the familiar Eq. 70 of Ref. 1.

Consider now the Case A ducts at the vertical asymptotes of Fig. 2 to 4. The slope dy/dx is $+\infty$ for Fig. 3 and $-\infty$ for Fig. 2 and 4. Thus, L of Fig. 12 starts at -0 at the x of the asymptote and at $+0$ in Fig. 11 and 13. For Case A, the sign of the correction term in Eq. 69 of Ref. 1 is the negative of that of L . Consider now the free bottom of Fig. 12. Here, L starts out at -0 and continues to grow large negatively. Thus, the third (correction) term starts out at zero and increases monotonically. This in turn causes the group velocity to be smaller than the result of Eq. 70 of Ref. 1.

The behavior is a bit more complicated for the rigid bottom of Fig. 11 and 13. Here, L starts at $+0$ and forms a positive relative maximum at the points of inflection of the curves of Fig. 2 and 4. It then crosses zero at $y = 0$. Thus, for the rigid bottom, the correction term is slightly negative for refracted rays, i.e., $y < 0$, and then turns increasingly positive for surface-reflected rays. The result is that the group velocity for refracted rays is generally somewhat larger than Eq. 70 of Ref. 1 and is less than Eq. 70 for surface-reflected rays. Here, there are two cases where Eq. 70 of Ref. 1 gives the group velocity: at infinite frequency corresponding to the vertical asymptote and for the ray which grazes the rigid bottom.

The foregoing analysis does not apply to mode 1A for the rigid-rigid condition of Fig. 13. Here, dy/dx goes to -1 at $x = 0$, $y = 0$ and L goes to 0.5 . In Fig. 10, we see that the phase-velocity curve has zero slope at zero frequency. Thus, from Eq. 63 of Ref. 1, we determine that in this case

$$C_g = C_p \quad (39)$$

or the group velocity in Fig. 16 is given by Eq. 36. One may also obtain Eq. 39 from Eq. 69 of Ref. 1 by noting that $L = 1/2$ and that Eq. 36 holds.

Consider now the Case B modes. Here, we can express Eq. 69 of Ref. 1 as

$$C_g = C_p [1 + (C_p^2 - C_2^2)/3C_2^2 + C_p^2(C_2^2 - C_1^2)(L - 1)/3]^{-1} \quad (40)$$

For the Case B profile configuration, one must consider a negative rather than positive half space, and the roles of C_1 and C_2 are reversed. For the Case B modes, Eq. 70 of Ref. 1 corresponds to Eq. 40, with the third term in the brackets suppressed. The third term of Eq. 40 may now be regarded as a corrective term to the result of Eq. 70 of Ref. 1.

At the horizontal asymptotes of Fig. 2 to 4, L approaches 1 from above in Fig. 2 and 3 for the free surface and from below in Fig. 4 for the rigid surface. For the free surface, $L - 1$ monotonically increases and the group velocity is smaller than Eq. 70 of Ref. 1. This is the same behavior as for Case A for the free bottom. The group velocity is given by Eq. 70 of Ref. 1 for infinite frequency, but falls progressively below the result of Eq. 70 as the frequency is decreased.

For the rigid surface of Fig. 4 and 13, $L - 1$ is negative for $x < 0$. There is a relative minimum in $L - 1$ at the point of inflection in Fig. 4, and it again crosses zero at $x = 0$ and continues to grow positive without bound as x is increased. Here again, the behavior is the same as for Case A for the rigid bottom. The group velocity equals that of Eq. 70 of Ref. 1 for infinite frequency and for the frequency corresponding to the ray which grazes the rigid bottom. Between these frequencies, the group velocity is larger than that of Eq. 70 of Ref. 1. For frequencies corresponding to surface-

reflected rays, the group velocity falls progressively below Eq. (70) of Ref. 1 as the frequency is decreased.

Again, the foregoing analysis does not apply to mode 1B for the rigid-rigid condition of Fig. 16. Here, L does not form a relative minimum, but decreases monotonically with increasing x to join with the mode 1A result at $x = 0$ and $y = 0$. Here, Eq. 39 applies for zero frequency.

Consider now some of the characteristics of Fig. 14 to 16. At high frequencies, C_g asymptotically approaches C_p . This follows from Eq. 69 of Ref. 1 for Case A modes as $C_p \rightarrow C_1$ and $L \rightarrow 0$. It follows from Eq. 40 for Case B modes as $C_p \rightarrow C_1$ and $L \rightarrow 1$. The limit of C_g for both Case A and B modes is 1480 m/s and follows from our choice of sample profiles.

As the frequency is decreased from large values, the group velocity increases and forms a relative maximum, the so-called Airy phase phenomenon, and then decreases rapidly as the frequency is lowered further. At the duct-cutoff frequencies, the group velocity goes to zero. This can be verified from Eq. 69 of Ref. 1 as $C_p \rightarrow \infty$ at the cutoff frequencies, and the third term in the brackets is positive.

Again, mode 1A in Fig. 16 has a different behavior. Here, there is a monotonic increase with decreasing frequency, with an end-point maximum at zero frequency given by Eq. 39 and 36.

The effect of the boundary condition on the group velocity is best illustrated by Fig. 14, where we see that the group velocity for Case B modes with the free surface lies well below the group velocity for Case A modes with the rigid surface. We can attribute this difference to two effects. We note that for values of C_p that are comparable to C_1 and C_2 , C_p appears as a multiplicative factor in Eq. 69 of Ref. 1. Thus, the first effect is the lower phase velocities in Fig. 8 for the Case B modes. We have already pointed out that the group velocity is greater than Eq. 70 of Ref. 1 for refracted rays for the rigid boundary. However, it is smaller than Eq. 70 of Ref. 1 for refracted rays for the free boundaries. This, then, is the second effect producing lower group velocities for the free boundaries.

The tendency for the free boundary to lower group velocities is also evident in Fig. 15, where the group velocity for both sets of modes is a relatively flat function of frequency, with the maximum group velocity rising slightly above 1480 m/s. In contrast, the group velocity for both sets of modes in Fig. 16 with rigid-rigid boundaries peaks significantly higher above 1480 m/s.

EIGENFUNCTION NORMALIZATION CONSTANTS

Before presenting numerical results, we need to simplify the general formulation of Ref. 1 so it will apply to a single layer. We will now present the theoretical expressions for all boundary conditions. For a single layer profile, Eq. 90 of Ref. 1 reduces to

$$D_c = D_s + D_b \quad (41)$$

Consider the free-rigid duct of Fig. 1. With the use of Eq. 81 of Ref. 1, the $F_i(Z)$ of Eq. 2 of Ref. 1 may be written as

$$F_1(Z) = Bi(-x) Ai(-x - a_1 Z) - Ai(-x) Bi(-x - a_1 Z) \quad (42)$$

From Eq. 73 and 81 of Ref. 1 and Eq. 1, we obtain

$$F_i(-\xi_{10}) = F_1(-y) = -G_1 \quad (43)$$

Equations 94 and 99 of Ref. 1 and Eq. 41 and 43 lead to

$$D_c = -\pi^{-2} + y(-G_1)^2 \quad (44)$$

Consider next the free-free duct. Equation 42 applies as is. From Eq. 73 and 76 of Ref. 1 and Eq. 2, we obtain

$$F_i'(-\xi_{10}) = F_1'(-y) = G_2 \quad (45)$$

Equations 94 and 98 of Ref. 1 and Eq. 41 and 45 lead to

$$D_c = -\pi^{-2} + G_2^2 \quad (46)$$

Consider now the rigid-rigid duct. With the use of Eq. 82 of Ref. 1, the $F_i(Z)$ may be written as

$$F_1(Z) = Bi'(-x) Ai(-x - a_1 Z) - Ai'(-x) Bi(-x - a_1 Z) \quad (47)$$

From Eq. 73 and 82 of Ref. 1 and Eq. 3, we obtain

$$F_i(-\xi_{10}) = F_1(-y) = -G_3 \quad (48)$$

Equations 95 and 99 of Ref. 1 and Eq. 41 and 48 lead to

$$D_c = -x\pi^{-2} + y(-G_3)^2 \quad (49)$$

Figures 17 to 19 present the respective results of Eq. 44, 46, and 49 for the canonical normalization coefficient. We will be pointing out various limits as x or y becomes large, whether negative or positive. The mathematical demonstrations of these limits are quite involved and are presented in Appendix C.

Note first that with one exception the curves never cross zero. This result was anticipated, because D_c equal to zero would correspond to the case where a mode is orthogonal to itself. This could happen in the case of degenerate eigenvalues, which cannot occur for a single layer duct. In point of fact, we were quite relieved when Fig. 17 to 19 were first generated, because had D_c crossed zero, we would have known that we had made an error in developing the theoretical expressions. Note, too, that the values for the A and B curves are always negative and positive, respectively.

The exceptional curves are 1A and 1B in Fig. 19, which hook together at $D_c = 0$ and $x = 0$. This corresponds to zero frequency. However, as will be discussed presently, this result leads to a nonzero value for D_n and apparently poses no problem.

All of the A and B curves approach zero asymptotically for large positive x . For large negative x , the B curves appear to increase without bound. Note that the A curves end abruptly at finite values of D_c and x . The horizontal line in Fig. 17 to 19 is $-\pi^{-2}$. The x corresponds to the vertical asymptotes in Fig. 2 to 4. The G_1 , G_2 , and G_3 of Eq. 44, 45, and 49, respectively, are messy indeterminate forms which go to zero in the limit. As a result, the limit of D_c goes to $-\pi^{-2}$ in Fig. 17 and 18, and to $-\pi^{-2}$ times the zeros of Ai' in Fig. 19. Mode 1A of Fig. 19 does not end on the horizontal line as do all the A modes of Fig. 17 and 18, but it comes close, because the first zero of Ai' is equal to 1.018. In the initial computer runs, these finite limits on the A curves were somewhat ragged. Double-precision calculations were then implemented to produce the clear-cut results of Fig. 17 to 19.

Figures 20 to 22 present the eigenvalue normalization coefficient for the respective curves of Fig. 17 to 19. These curves were generated by Eq. 89 of Ref. 1 by using the specific profile parameters already discussed. Consider first the A curves, which appear well-behaved. Appendix C demonstrates that they all go to zero for infinite frequency. Note that the curves of Fig. 20 and 21 appear to merge to a common curve for high frequency. This is an intriguing result, but we are not inclined to tackle the theoretical analysis in this article.

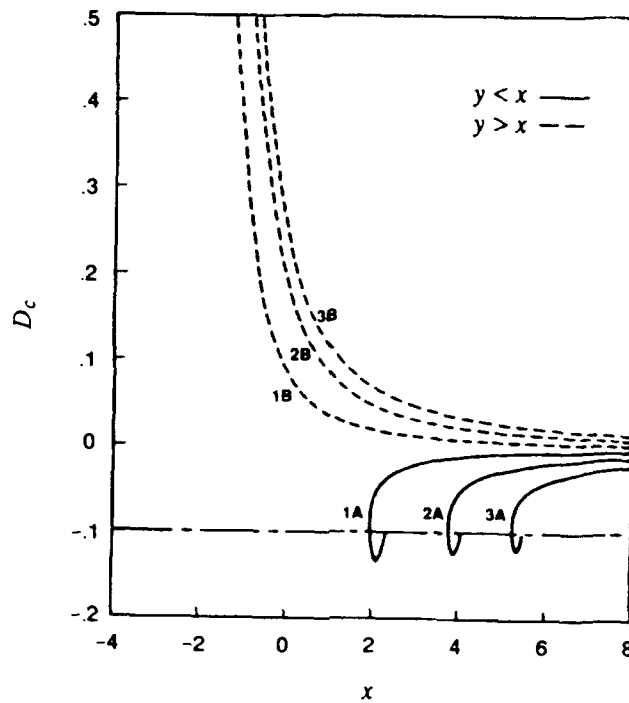


Figure 17. Canonical normalization coefficient for the free-rigid boundaries.

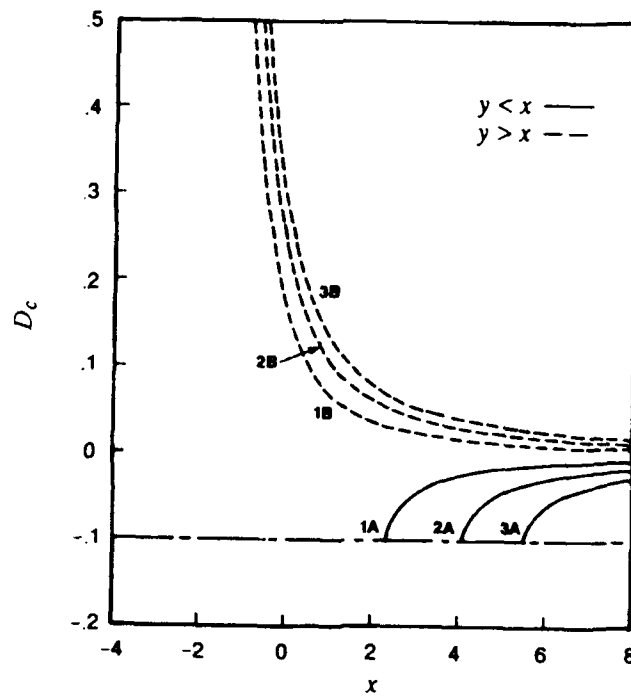


Figure 18. Canonical normalization coefficient for the free-free boundaries.

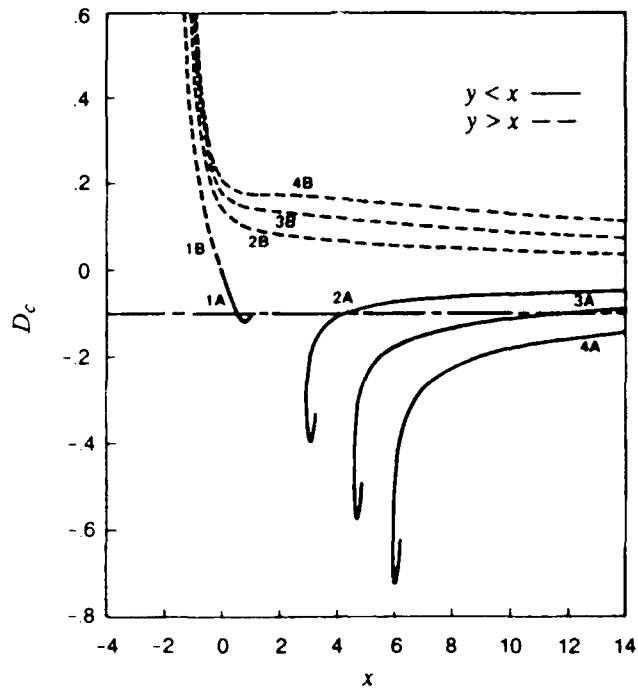


Figure 19. Canonical normalization coefficient for the rigid-rigid boundaries.

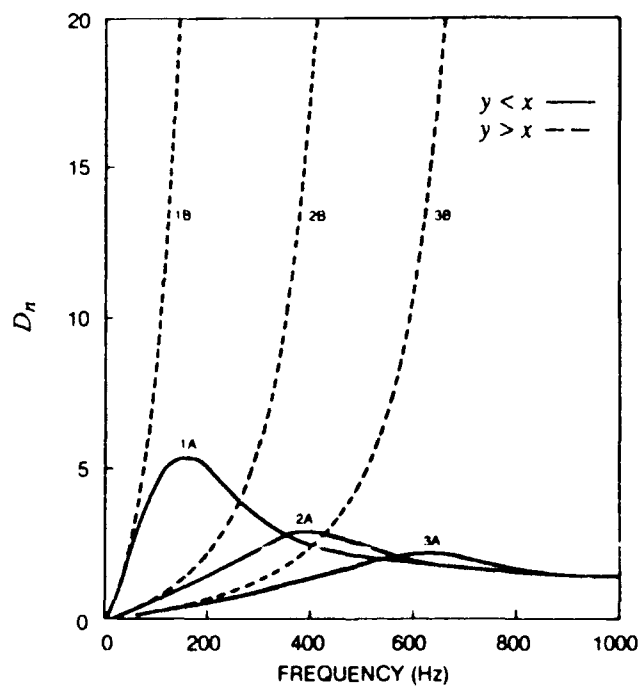


Figure 20. Eigenvalue normalization coefficient for the free-rigid boundaries.

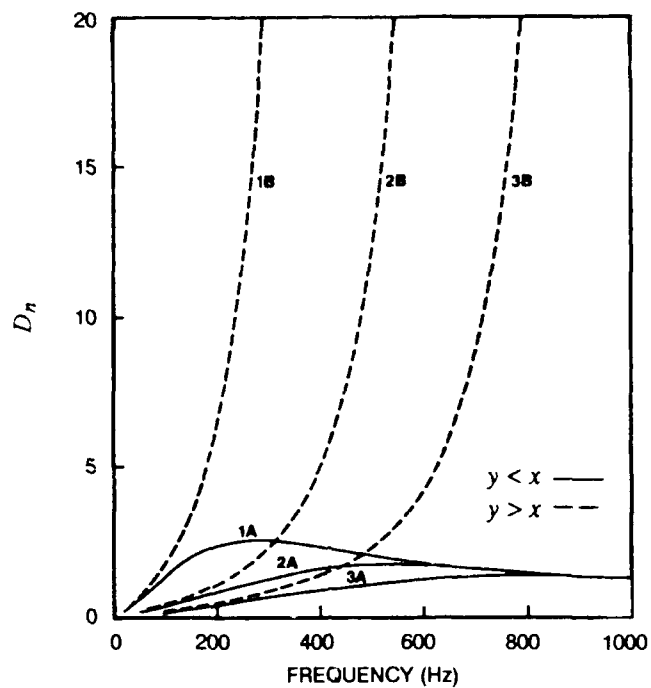


Figure 21. Eigenvalue normalization coefficient for the free-free boundaries.

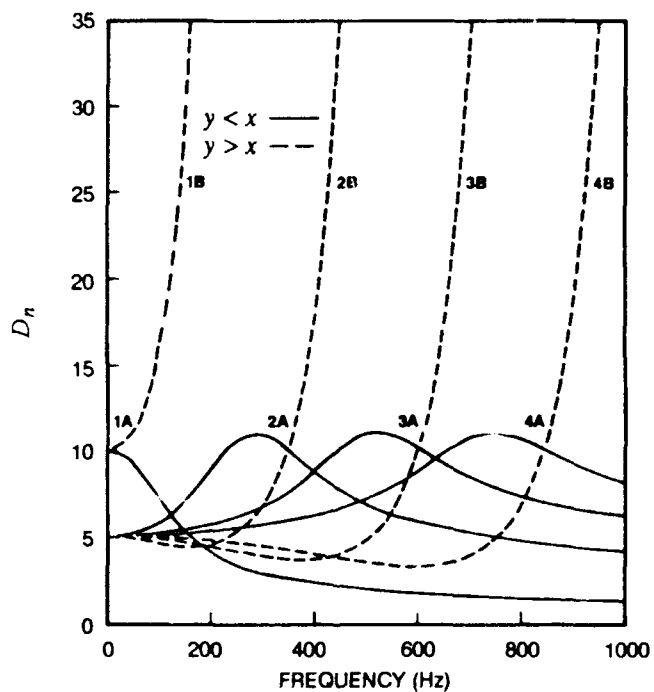


Figure 22. Eigenvalue normalization coefficient for the rigid-rigid boundaries.

Consider now the limits of D_n as the frequency is decreased to small values. Appendix C demonstrates that for the free-rigid and free-free boundaries of Fig. 20 and 21, respectively, D_n goes to zero at the duct cutoff frequencies. However, for the rigid-rigid boundary of Fig. 22, D_n for modes 1A and 1B at zero frequency goes to a finite, nonzero, value of $Z_2\pi^{-2}$, where Z_2 is the duct thickness. This result is also demonstrated in Appendix C. The limit of D_n at the cutoff frequencies for both A and B curves for mode 2 and higher-order modes is apparently $Z_2\pi^{-2}/2$. We say *apparently* because a rigorous proof of this result is extremely difficult, and the discussion of this result in Appendix C is theoretically on somewhat shaky ground.

The numerical values of the examples of Fig. 22 are 5.06 and 5.08 m for modes 2 and above for Cases A and B, respectively, with double these values for modes 1A and 1B, respectively. Difficulties with the analysis of Appendix C led us to question at one time whether the numerical results for modes 2A, 3A, and 4A in Fig. 22 were correct. However, the result for 1A and 1B is on firm ground theoretically, and since the relative maximum of 2A, 3A, and 4A line up well with the 1A result, we cannot fault the numerical result. The results point up the fact that D_n in Fig. 20 to 22 is a quantity with dimensions of meters. If one carries out the process forward to the point of evaluating propagation losses, these losses are then referenced relative to 1 m.

Whereas the normalization process appears to work well for the A family of modes, the rapid increase with frequency for the B family of modes makes this approach unattractive. We were prompted to examine an alternative method of normalization based on the boundary condition at the bottom rather than at the surface. An alternative expression for Eq. 42 is

$$F_1(Z) = Bi'(-y) Ai(-x + a_1Z) - Ai'(-y) Bi(-x + a_1Z) \quad (50)$$

Here, the coefficients D_1 and E_1 have been chosen to satisfy the bottom boundary condition for a rigid bottom. Equation 50 also applies to the rigid-rigid duct. The counterpart of Eq. 50 for the free-free duct is

$$F_1(Z) = Bi(-y) Ai(-x + a_1Z) - Ai(-y) Bi(-x + a_1Z) \quad (51)$$

With this alternative method, the counterparts of Eq. 44, 46, and 49 become, respectively

$$D_c = y\pi^{-2} - (-G_4)^2 \quad (52)$$

$$D_c = \pi^{-2} - (-G_3)^2 \quad (53)$$

and

$$D_c = y\pi^{-2} - x G_2^2 \quad (54)$$

Figures 23 to 25 present the respective results of Eq. 52 to 54. In common with Fig. 17 to 19, the values of D_c are positive for the B family and negative for the A family. The results also go to zero for large values of x . In contrast to Fig. 17 to 19, the behavior of the A and B families is reversed. Here, the B family goes to fixed limits for large negative x , while the A family diverges by forming vertical asymptotes as y goes to minus infinity in Fig. 2 to 4. Here, the G_4 , G_3 , and G_2 of Eq. 52 to 54, respectively, go to zero in the limit. As a result, the limit of D_c goes to π^{-2} times the zeros of Ai' in Fig. 23 and 25 and to π^{-2} in Fig. 24.

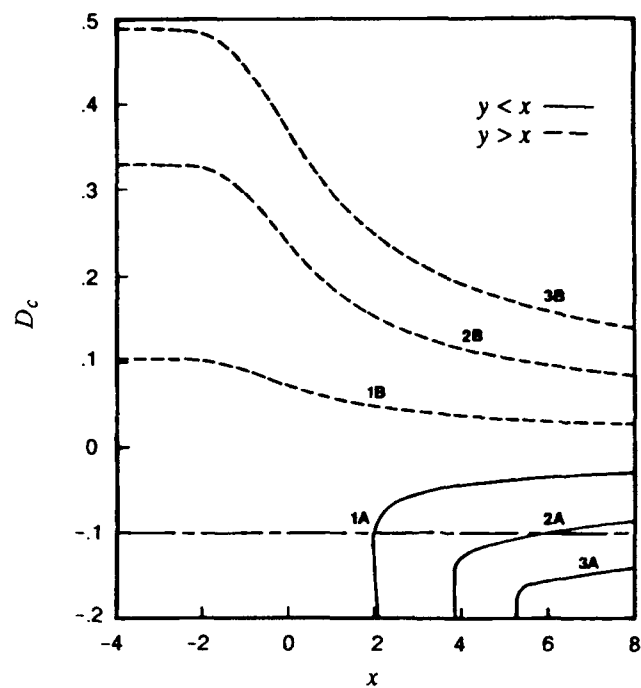


Figure 23. Counterpart of Fig. 17 for alternative normalization.

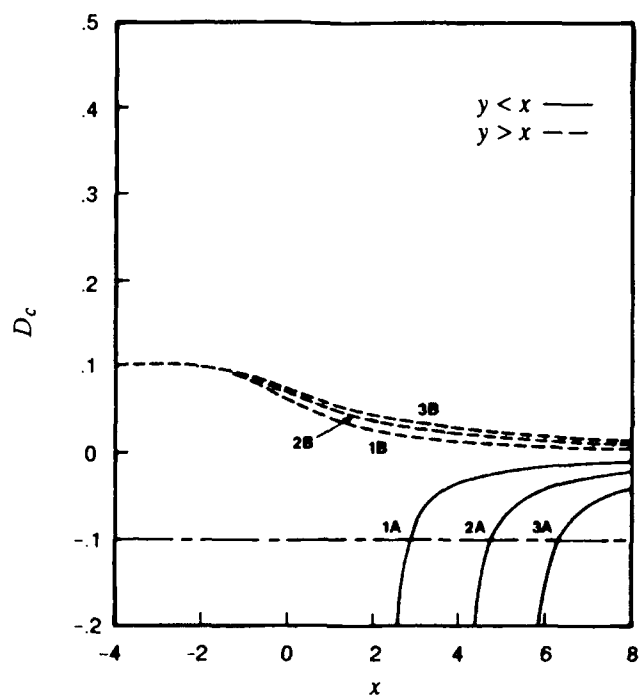


Figure 24. Counterpart of Fig. 18 for alternative normalization.

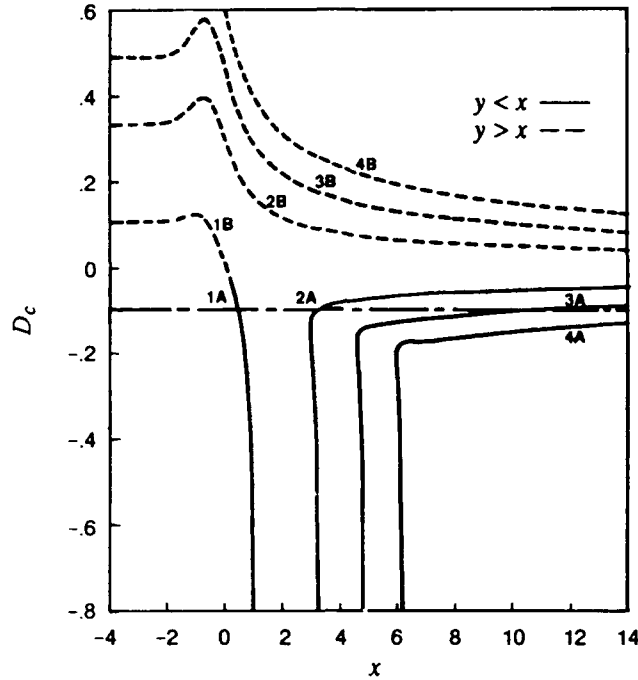


Figure 25. Counterpart of Fig. 19 for alternative normalization.

Figures 26 to 28 present the eigenvalue normalization coefficient for the respective curves of Fig. 23 to 25. We see that the alternative approach to normalization has achieved the desired goal. Here, the Case B modes are all well behaved, although the Case A modes now increase rapidly with increasing frequency. The opposite behavior of Case A and B modes is discussed further in Appendix C.

In closing this section, we note that the dashed and solid curves of Fig. 21 are almost identical to the solid and dashed curves, respectively, of Fig. 27. The same property holds for Fig. 22 and 28. The choice of profile parameters is such that if we turn the free-free or rigid-rigid profiles upside down, we have almost the same physical problem, with the roles of the A and B families reversed. The same physical problem should produce the same results, despite the fact that the two approaches are quite different. We will not attempt to demonstrate theoretically that the two formulations lead to the same result, because such a demonstration appears very involved. For example, there is small resemblance between the intermediate results of Fig. 19 and 25. Yet the final results of Fig. 22 and 28 agree. We were pleased at the result, because it tends to increase our confidence that the normalization process has been properly implemented. For the phase- and group-velocity plots of Fig. 8 to 10 and Fig. 14 to 16, we had enough experience with the customary eigenvalue approach to recognize that the canonical approach was producing familiar patterns. In contrast, we had no such experience with plots of D_n as a function of frequency, and hence had little feel for what the characteristics of Fig. 20 to 22 or 26 to 28 should be.

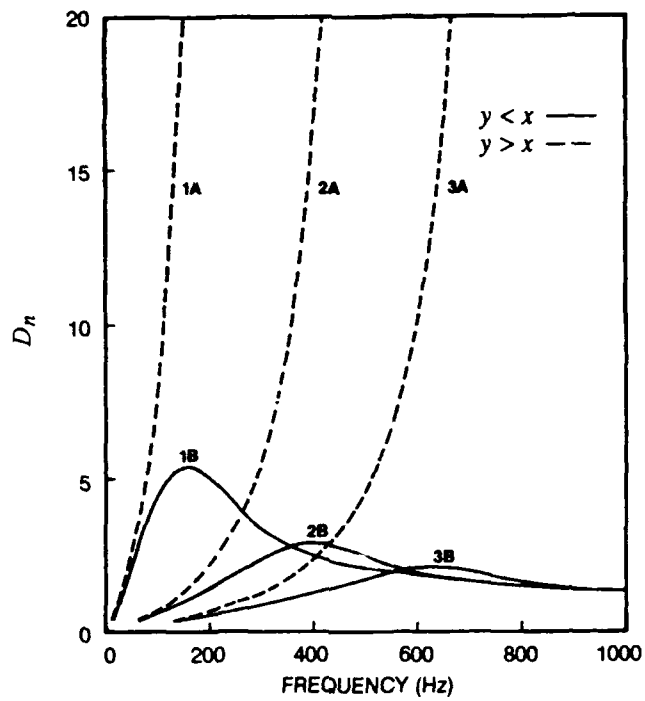


Figure 26. Counterpart of Fig. 20 for alternative normalization.

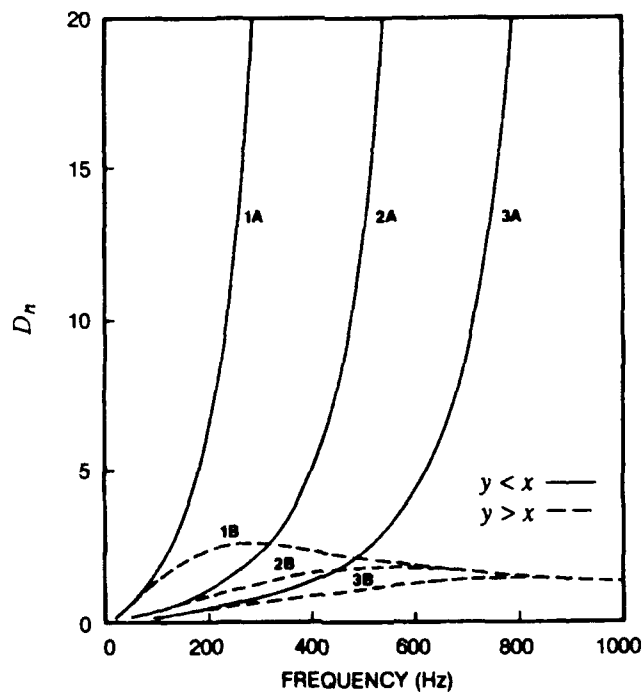


Figure 27. Counterpart of Fig. 21 for alternative normalization.

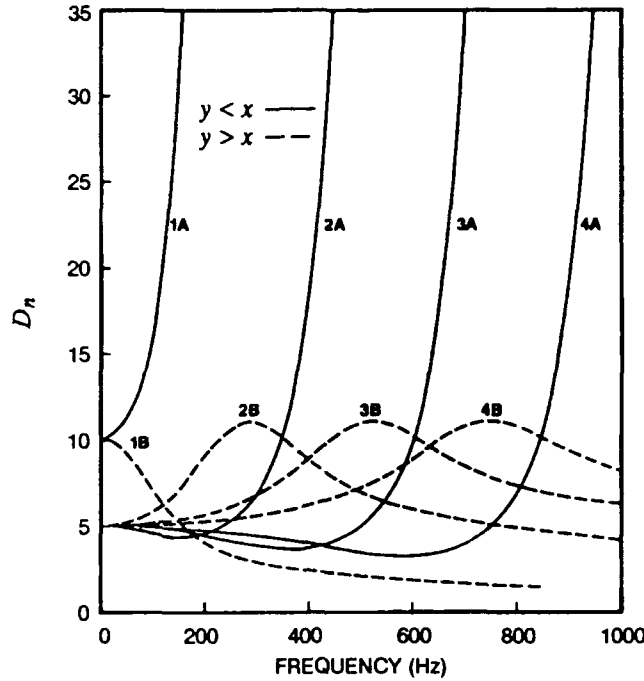


Figure 28. Counterpart of Fig. 22 for alternative normalization.

As this report was about to be submitted for publication, some numerical results on two-layer bounded profiles became available. These results suggested that the normalization curves for the B modes in Fig. 17 to 19 may not diverge for negative values of x . The case of Fig. 17 was investigated in more detail, and it was found that for mode 1 a relative maximum in D_c occurred at $x = -8.9$, with a value of $D_c = 3.8 \times 10^{14}$. Furthermore, this result implies that D_n in Fig. 20 to 22 does not diverge at large frequencies but forms a relative maximum. The result indicates that the limit analysis attempted in Appendix C is even more difficult than believed when Appendix C was prepared. The question of whether D_c and D_n diverge for the B modes is somewhat moot, since the alternative normalization of Eq. 50 to 54 eliminates the problem.

SUMMARY

The application of the theory of canonical eigenvalues to underwater sound propagation in a one-layer bounded duct has more than lived up to the expectations we had for it. This application demonstrates not only the general advantages cited in Ref. 1, but also some new advantages. It has also produced a number of specific results of importance or interest. This section is a summary of these advantages and specific results, presented for the most part in the order in which they arose in the approach.

The method reduces the number of parameters in the customary eigenvalue equation by four. The four parameters eliminated are C_1 , C_2 , γ_1 and f . For a one-layer bounded duct, this leaves no parameters in the canonical eigenvalue equation. Thus, the eigenvalue solutions apply to all possible sound-speed profiles with the given boundary condition.

The canonical eigenvalue curves pass through two sets of lattice points, which are known solutions to the eigenvalue equation and are obtained from zeros to various Airy functions. For reflection from both layer boundaries, these lattice points almost delineate the eigenvalue curves. Of particular importance are the zeros at minus infinity, which define the vertical asymptotes for the Case A modes and the horizontal asymptotes for the Case B modes. These asymptotes provide important characteristics of the propagation at high frequencies for refracted rays which reflect from only one boundary.

The near-uniform spacing between the set of A and B modes (and of the line $y = x$ when it is a solution) is an example of the mathematical essence of the solution. This spacing provides a clue to the location of mode 1, which is not available in the customary approach.

The plots of phase velocity vs frequency exhibited the familiar characteristic of diverging at low frequency and asymptotically approaching the lower of the boundary sound speeds at high frequency. This divergence is related to a low-frequency cutoff, which detailed analysis demonstrated could be given by duct thickness, expressed in terms of acoustic wavelength.

The expression for group velocity contains the sum of three terms. The first two terms can be associated with the classic result of ray theory, while the third term is a "tweaking" term which is a function of the slope of the eigenvalue curves. This expression is not only appealing from a theoretical standpoint, it is also simpler to apply than the formulation used in the customary normal-mode approach. The group velocities for refracted rays, forming a vertex below a free surface or a nadir above a free bottom, are significantly smaller than their counterparts for a rigid surface or rigid bottom. This result is associated with the fact that the tweaking term in the group velocity is positive for free or negative for rigid boundary conditions.

The plots of group velocity vs frequency exhibited the familiar behavior of going to zero at low frequencies and approaching the lower of the boundary sound speeds from above at high frequency. A relative maximum, the Airy phase, is formed for intermediate frequencies.

The profile parameters were chosen in such a manner that the physical solutions for Case A and Case B should be almost identical when the surface and bottom boundary conditions are the same. This can be inferred from the fact that here Case B can be obtained by turning the Case A profile upside down. For free-free and rigid-rigid boundary conditions, the Case A and B solutions for phase and group velocity were indeed almost identical, even though the intermediate results (such as eigenvalues or canonical group velocity factor) were markedly different for Case A and Case B.

The eigenvalue curve for mode 1 of Case A and Case B for the rigid-rigid boundary condition was radically different from that of any other mode for any of the boundary conditions. However, an unusual pattern could be inferred from the lattice points and the locus of the higher-order eigenvalues. Further investigation demonstrated that this solution was not only mathematically correct, but also

led to phase and group velocities which made sense physically. Here, mode 1 corresponds to a subset of refracted rays which do not reflect from both surfaces. In contrast to all other modes, there is no low-frequency cutoff. The phase and group velocities go to a finite, nonzero value at zero frequency. The square of this value is the harmonic mean square of the sound speeds at the two boundaries. This value is slightly less than the arithmetic mean of the two sound speeds.

The bulk of the eigenfunction normalization process can be carried out in terms of the canonical eigenvalues to evaluate the canonical eigenfunction normalization coefficient. This coefficient applies to the entire class of profiles represented by the eigenvalue solution. The eigenfunction normalization coefficient for a specific profile of the class is obtained by a simple function which scales the canonical coefficient. This approach is more straightforward than the customary approach.

The standard approach to selecting eigenfunction coefficients, before normalization, by satisfying the surface boundary condition worked well for the Case A modes. However, the Case B mode normalization became very large for higher frequencies. An alternative approach was implemented in which the bottom rather than surface boundary condition was satisfied. Here, the Case A and B roles were reversed, with a satisfactory result for the Case B mode, whereas the Case A mode became very large for higher frequencies. For the free-free and rigid-rigid boundary conditions, the eigenvalue normalization coefficients for Case A (and Case B) for the standard approach were almost identical to those for Case B (and Case A), even though intermediate results (such as the canonical normalization factor) were drastically different.

The plots of the eigenfunction normalization coefficients vs frequency exhibit a characteristic pattern. The values are always positive. The coefficient goes to zero at the cutoff frequencies for the free-rigid and free-free boundary conditions. For the rigid-rigid boundary condition, the coefficient goes to $\pi^2 Z_2 / 2$ for the cutoff frequencies for modes 2 and above. Here, Z_2 is the duct thickness. At zero frequency, the coefficient goes to $\pi^2 Z_2$ for mode 1 for the rigid-rigid boundary condition. With the exception of this mode, all other modes for all boundary conditions form a relative maximum at intermediate frequencies. At high frequencies, all modes asymptotically go to zero. For the rigid-rigid and free-free boundary conditions the curves for the various modes appear to merge to a common curve at high frequencies.

REFERENCES

1. Pedersen, M. A., D. F. Gordon, and F. Hosmer, "Canonical Eigenvalues, Part I: General Theory," Naval Ocean Systems Center, San Diego, CA, NOSC TR 1332, Feb 1990.
2. Abramowitz, M., and I. A. Stegun, *Handbook of Mathematical Functions*, National Bureau of Standards Applied Mathematics Series 55, Ninth Printing, 1970.
3. Churchill, R. V., *Fourier Series and Boundary Value Problems*, McGraw-Hill, New York and London, 1941.
4. Pedersen, M. A., D. F. Gordon, and F. Hosmer, "Phase and Group Velocities for Normal-Mode and Phase-Integral Approaches in Simple Underwater Acoustic Ducts," Naval Ocean Systems Center, San Diego, CA, NOSC TR 1331, Jan 1990.

Appendix A

COMPARISON OF PHASE VELOCITY FOR CASE A AND CASE B

This appendix demonstrates that the phase velocity vs frequency curves are almost identical for Case A and Case B in Fig. 9 and 10. Let the variables and parameters for Case A be given by x , y , C_1 , C_2 , and γ_1 . Let barred values represent the corresponding values for Case B. The Case B values are related to Case A values as follows:

$$\bar{x} = y ; \bar{y} = x \quad (\text{A-1})$$

$$\bar{C}_1 = C_2 ; \bar{C}_2 = C_1 ; \bar{\gamma}_1 = -\gamma_1 \quad (\text{A-2})$$

Equation A-1 holds because the curves of Fig. 3 and 4 are symmetric about the line $y = x$. Equation A-2 holds because of our choice of sample profiles for Case A and Case B.

We now compare the f of Eq. 14 of Ref. 1 for the Case A values with the \bar{f} of Eq. 14. Substituting Eq. A-1 and A-2 into the right side of Eq. 14, we obtain the following relationship:

$$\bar{f} = f(C_1/C_2)^3 \quad (\text{A-3})$$

If we now substitute Eq. A-1 to A-3 into the right side of Eq. 17 of Ref. 1, we obtain

$$\bar{C}_p = C_2 [1 - \pi^{-2/3} \bar{f}^{2/3} |\gamma_{10}|^{2/3} y]^{-1/2} \quad (\text{A-4})$$

A comparison of Eq. A-4 with Eq. 30 yields the desired result that

$$\bar{C}_p = C_p \quad (\text{A-5})$$

Appendix B

DUCT CUTOFF FREQUENCIES

In this appendix, we obtain expressions for the duct cutoff frequencies expressed in terms of wavelength. We first note that

$$f = N_0 C_1 Z_2^{-2} \quad (\text{B-1})$$

expresses frequency, where N_0 is the number of vertical wavelengths in the duct, C_1 is the surface sound speed, and Z_2 is the duct thickness. Our problem is to obtain expressions for N_0 at the cutoff frequency of the duct.

From Eq. 1 of Ref. 1, we determine that

$$C_1 Z_2^{-1} = -2\gamma_1 (C_1^2 C_2^{-2} - 1)^{-1} \quad (\text{B-2})$$

It follows then from Eq. B-1 and B-2 and from Eq. 14 of Ref. 1 that

$$N_0 = \pm (y-x)^{3/2} (C_1^2 C_2^{-2} - 1)^{-1/2} (2\pi)^{-1} \quad (\text{B-3})$$

The plus sign holds for Case B and the minus sign for Case A. Equation B-3 holds for any frequency.

We next determine the conditions corresponding to the cutoff frequencies. The cutoff frequencies occur when C_p of Eq. 17 of Ref. 1 goes to infinity. This occurs when

$$f^{2/3} = \pi^{-2/3} |\gamma_1|^{2/3} x \quad (\text{B-4})$$

We now take the two-thirds power of Eq. 14 of Ref. 1, equate to Eq. B-4, and simplify to determine that

$$x = (y-x) (C_1^2 C_2^{-2} - 1)^{-1} \quad (\text{B-5})$$

We take the one-half power of Eq. B-5 and substitute into Eq. B-3 to obtain

$$N_0 = \pm (y-x) x^{1/2} (2\pi)^{-1} \quad (\text{B-6})$$

where the plus sign holds for Case B and the minus sign for Case A.

Consider now the lattice points of Eq. 6 and 7 for the free-rigid boundary condition. Let the point be at the n_1 zero of Eq. 6 and the n_2 zero of Eq. 7. We consider the first term of the asymptotic expansion of $Ai(-x)$ as given by section 10.4.60 of Ref. 2. If we set this term to zero, we find that

$$(2/3)x^{3/2} = \pi(n_1 - 1/4) \quad (\text{B-7})$$

or

$$x = (3\pi/2)^{2/3} n_1^{2/3} (1 - 1/4n_1)^{2/3} \quad (\text{B-8})$$

We next consider the first term of the asymptotic expansion of $Ai'(-y)$ as given by section 10.4.62 of Ref. 2. The counterparts of Eq. B-7 and B-8 are

$$(2/3)y^{3/2} = \pi(n_2 - 3/4) \quad (\text{B-9})$$

and

$$y = (3\pi/2)^{2/3} n_2^{2/3} (1 - 3/4n_2)^{2/3} \quad (\text{B-10})$$

Consider the Case A modes. Here

$$n = n_1 - n_2 + 1 \quad (\text{B-11})$$

where n is the mode number. Equation B-11 may be verified by noting in Fig. 2 the relationship between mode number and lattice point.

We next use the binomial expansion on the last factor of Eq. B-8 to obtain

$$x = (3\pi/2)^{2/3} (n_1^{2/3} - n_1^{-1/3}/6) \quad (\text{B-12})$$

We use Eq. B-11 to express n_2 in terms of n_1 and n and use the binomial expansion twice—once on each of the last two factors of Eq. B-10 to obtain

$$y = (3\pi/2)^{2/3} [n_1^{2/3} + 2(1-n)n_1^{-1/3}/3](1 - n_1^{-1}/2) \quad (\text{B-13})$$

We expand Eq. B-13 and subtract Eq. B-12 to obtain

$$y - x = (3\pi/2)^{2/3} n_1^{-1/3} (1 - 2n)/3 \quad (\text{B-14})$$

The substitution of Eq. B-12 and B-14 into Eq. B-6 yields the final result:

$$N_0 = (2n - 1)/4 \quad (\text{B-15})$$

Consider next the B family of modes for the free-rigid condition. The demonstration is quite similar, with minor changes, as will now be noted. The counterpart of Eq. B-11 is

$$n = n_1 - n_2 \quad (\text{B-16})$$

This results in the $(1-n)$ factor in Eq. B-13 being replaced by n . This in turn yields the negative of Eq. B-14, and the result of Eq. B-15 is the same for Case B as for Case A.

We next treat the free-free boundary condition for which the lattice points are given by Eq. 13 and 14 and for the Case A modes. Equation B-12 applies for x and it also applies for y with n_1 replaced by n_2 . The counterpart of Eq. B-11 is

$$n = n_1 - n_2 \quad (\text{B-17})$$

The counterpart of Eq. B-13 is

$$y = (3\pi/2)^{2/3} [n_2^{2/3} - 2nn_2^{-1/3}/3](1 - n_2^{-1}/6) \quad (\text{B-18})$$

This results in the $(1-2n)$ factor of Eq. B-14 being replaced by $(-2n)$. The counterpart of Eq. B-15 then becomes

$$N_0 = n/2 \quad (\text{B-19})$$

We next treat the rigid-rigid boundary condition for which the lattice points are given by Eq. 20 and 21 and for the Case A modes. Equation B-10 applies for y and it also applies for x , with n_2 replaced by n_1 . The counterpart of Eq. B-12 is

$$x = (3\pi/2)^{2/3} (n_1^{2/3} - n_1^{-1/3}/2) \quad (\text{B-20})$$

The counterpart of Eq. B-11 is the same as Eq. B-11. Thus, Eq. B-13 applies for this case. This results in the $(1 - 2n)$ factor in Eq. B-14 being replaced by $2(1 - n)$. The counterpart of Eq. B-15 for this case reduces to

$$N_0 = (n - 1)/2 \quad (\text{B-21})$$

For the Case B modes for the free-free and rigid-rigid boundaries, the signs on n_1 and n_2 are the reverse of that in Eq. B-17 and B-11, respectively. This results in a sign reversal on the expressions for $x - y$. Thus N_0 for the Case B modes reduces to the same expression as that for the Case A modes for both sets of boundary conditions.

Before closing this appendix, a few comments on the derivation are in order. The reason that the analysis is so intricate and involved is that a number of indeterminate forms must be dealt with. For example, in Eq. 14 of Ref. 1, we must deal with the form $\infty - \infty$ as both x and y increase without bound. Equation B-14 and its counterparts for other boundary conditions all contain the factor $n_1^{-1/3}$. Thus, we see that as n_1 increases without bound, the frequency goes to zero. Since the lattice points lie on the curve, it follows that the frequency for arbitrary x and y must go to zero for x and y without bound. We chose the lattice points associated with the zeros of A_i and A_i' . Alternatively, we could have conducted the analysis on the lattice points associated with the zeros of B_i and B_i' . This analysis would have lead to the same result.

Thus, Eq. B-14 demonstrates our statement in the main text that the canonical frequency plots go to zero asymptotically as x becomes large without bound.

The evaluation of Eq. B-6 involves another indeterminate form of the type zero times infinity. In this case, $y - x$ depends on n_1 as $n_1^{-1/3}$, whereas the dependence of $x^{1/2}$ on n_1 is as $n_1^{1/3}$. The result is that N_0 in Eq. B-15, B-19, or B-21 is a finite nonzero constant.

We apparently achieved the result without explicitly letting n_1 become arbitrarily large. However, this is implicit in the proof, because the analysis is based only on the first term of the asymptotic expansions of A_i and A_i' and only on the first two terms of the various binomial expansions.

In closing, Eq. B-3 applies for any x, y solutions of the eigenvalue equation. However, Eq. B-6 does not. It only applies at the cutoff frequencies as given by the condition of Eq. B-5.

Appendix C

LIMITS OF THE VARIOUS NORMALIZATION COMPONENTS

Our first task is to investigate the limits of the various expressions for D_c given in the main text. Consider, for example, G_1 of Eq. 44. The analysis is facilitated by a simplification of Eq. 1. We solve the eigenvalue equation, Eq. 2 and 5 for $Bi(-x)$, substitute for $Bi(-x)$ in Eq. 1 and simplify. The result is

$$G_1 = -\pi^{-1} Ai(-x)/Ai'(-y) \quad (C-1)$$

We treat the G functions of Eq. 46, 49, 52, 53, and 54 in the same manner, using the appropriate eigenvalue equation to simplify the expression, and obtain, respectively

$$G_2 = \pi^{-1} Ai(-x)/Ai'(-y) \quad (C-2)$$

$$G_3 = -\pi^{-1} Ai'(-x)/Ai'(-y) \quad (C-3)$$

$$G_4 = -\pi^{-1} Ai'(-y)/Ai(-x) \quad (C-4)$$

$$G_5 = -\pi^{-1} Ai'(-y)/Ai(-x) \quad (C-5)$$

and

$$G_6 = \pi^{-1} Ai(-y)/Ai'(-x) \quad (C-6)$$

The limits of Eq. C-1 to C-6 are much easier to evaluate than the original expressions of Eq. 1 to 4. Indeed, in the computer program, Eq. C-1 to C-5 were used to reduce the effect of numerical roundoff.

Consider now the limits for large positive x and y . Here $y \rightarrow x$ asymptotically and the Airy function ratios in Eq. C-2, C-3, C-5, and C-6 go to 1. From Sections 10.4.59 and 10.4.61 of Ref. 2, the Airy function ratio in Eq. C-1 goes to $-(xy)^{-1/4}$ and to $-(xy)^{1/4}$ in Eq. C-4. It is evident then that the second terms of Eq. 44 and 46 go to π^{-2} , the second term of Eq. 49 goes to $y\pi^{-2}$, the second term of Eq. 52 and 54 goes to $-x\pi^{-2}$, and the second term of Eq. 53 goes to $-\pi^{-2}$. Thus, Eq. 44, 46, and 53 reduce to

$$\pi^{-2} - \pi^{-2} = 0 \quad (C-7)$$

whereas Eq. 49, 52, and 54 reduce to

$$x(\pi^{-2} - \pi^{-2}) = 0 \quad (C-8)$$

It is of interest that as x becomes large positive, Fig. 17, 18, and 24 approach zero much faster than do Fig. 19, 23, and 25. The reason is that the former three correspond to Eq. C-7. The latter three correspond to Eq. C-8, in which the difference of functions not only must cancel each other as in Eq. C-7, but also must drag down the multiplier x of Eq. C-8.

We next examine the limits for large negative x or y . Recall that for the Case A modes, x goes to the zeros of $Ai(-x)$ or $Ai'(-x)$ as y goes to minus infinity; whereas for the Case B modes, y goes to the zeros of $Ai(-y)$ or $Ai'(-y)$ as x goes to minus infinity. Thus, Eq. C-1 to C-6 are all indeterminate forms of the type 0/0.

We have attempted to evaluate these forms by applying L' Hospital's rule without success. This procedure is complicated, because it involves dy/dx , and one differentiation did not provide the answer. However, we will make one relatively simple assumption and then demonstrate that all of the numerical results are compatible with this assumption. The assumption is that a finite zero of an Airy function goes to zero faster than does the zero at x or y equal to minus infinity.

This assumption leads to zero and infinity as the limits of Eq. C-1 to C-3 for Case A and Case B modes, respectively. This is compatible with the results of Fig. 17 to 19, in which the Case A modes go to finite limits and the Case B modes appear to diverge. Eq. C-4 to C-6 involve the reciprocals of the right sides of Eq. C-1 to C-3, respectively. Thus, the roles are reversed, and the assumption leads in Fig. 23 to 25 to finite limits for Case B and apparently divergent values for Case A.

We next examine the limits of D_n for high frequency. This involves the limits of D_c as x or y goes to minus infinity, as just discussed. For those cases in which D_c has a finite limit, it is clear from Eq. 89 and from Eq. 4 of Ref. 1 that D_n goes to zero as suggested by the A modes in Fig. 20 to 22 and the B modes in Fig. 26 to 28. Apparently the $f^{2/3}$ dependence in a_1^{-1} is not strong enough to drag down a divergent D_c . Thus, D_n apparently diverges for the B modes in Fig. 20 to 22 and for the A modes in Fig. 26 to 28.

Our final task is to examine the limits of D_n as the frequency decreases to low values. From Eq. 14 of Ref. 1 and Eq. B-2, it follows that

$$f^{2/3} = -(y-x)C_1 Z_2^{-1} \gamma_1^{-1/3} \pi^{-2/3}/2 \quad (C-9)$$

Substitution into Eq. 4 of Ref. 1 leads to

$$a_1 = (y-x)Z_2^{-1} \quad (C-10)$$

Thus

$$D_n = Z_2 D_c/(y-x) \quad (C-11)$$

D_c is of the form π^{-2} (zero) for the free-rigid and free-free boundary conditions and $\pi^{-2}(y-x)$ for the rigid-rigid boundary conditions.

Consider now the case of the modes 1A and 1B for the rigid-rigid boundary condition. Here, $x = -y$ at low frequencies and x approaches zero. The result then appears to reduce to

$$D_n = Z_2 \pi^{-2} \quad (C-12)$$

which is the limit shown in Fig. 22.

However, for higher-order modes, $x \rightarrow y$ asymptotically. A similar analysis appears to give the same answer as Eq. C-12. However, the numerical limit shown in Fig. 22 is one half of Eq. C-12. We puzzled over this result until we recognized that at duct cutoff, Eq. B-4 holds. If we use Eq. B-4 to evaluate a_1 , we obtain

$$a_1 = -2 \gamma_1 x/C_1 \quad (C-13)$$

For the free-rigid and free-free boundary conditions

$$D_n = -C_1 \pi^{-1} (\text{zero})/2 \gamma_1 x \quad (C-14)$$

As x goes to infinity, Eq. C-14 goes to zero, in agreement with Fig. 20 and 21. For the rigid-rigid boundary condition

$$D_n = -C_1 \pi^{-2}(y-x)/2 \gamma_1 x \quad (C-15)$$

Here, as y approaches x , the limit of Eq. C-15 appears to go to zero, which does not agree with Fig. 22.

The problem here is that Eq. C-15 does not take into account that Eq. B-6, as well as Eq. B must hold. If for the rigid-rigid condition, the limit of D_c as y approaches x asymptotically is

$$D_c = \pi^{-2}(y-x)/2 \quad (C-16)$$

and the result of Fig. 22 is obtained. The proof of Eq. C-16 appears to require an analysis of lattice points similar to that of Appendix B and appears too difficult to attempt here.

In the discussion following Eq. B-4, it was noted that the standing wave for the rigid-rigid bottom at cutoff was approximated by a cosine function. If one normalizes this cosine function, one obtains, $Z_2/2$ as the normalization. The Airy functions involve a factor of π^{-1} times the trigonometric functions. This leads to the desired result:

$$D_n = Z_2 \pi^{-2}/2 \quad (C-17)$$

Although the various limits of D_c and D_n are of interest as a mathematical challenge, our primary reason for the analysis in this appendix was a verification of the numerical results. We wish to guard against possible error in the numerical implementation of the theory. Whereas our mathematical analysis leaves some significant unresolved gaps, there are enough points of agreement to make us reasonably certain that the numerical results are not in error.

REPORT DOCUMENTATION PAGE

Form Approved
OMB No. 0704-0188

Public reporting burden for this collection of information is estimated to average 1 hour per response, including the time for reviewing instructions, searching existing data sources, gathering and maintaining the data needed, and completing and reviewing the collection of information. Send comments regarding this burden estimate or any other aspect of this collection of information, including suggestions for reducing this burden, to Washington Headquarters Services, Directorate for Information Operations and Reports, 1215 Jefferson Davis Highway, Suite 1204, Arlington, VA 22202-4302, and to the Office of Management and Budget, Paperwork Reduction Project (0704-0188), Washington, DC 20503.

1. AGENCY USE ONLY (Leave blank)		2. REPORT DATE June 1990		3. REPORT TYPE AND DATES COVERED March 1986-September 1989	
4. TITLE AND SUBTITLE CANONICAL EIGENVALUES: Part II. Application to One-Layer, Bounded, Underwater Acoustic Ducts				5. FUNDING NUMBERS 061152N R00N0 71ZW0901	
6. AUTHOR(S) Melvin A. Pedersen, David F. Gordon, and Fell Hosmer					
7. PERFORMING ORGANIZATION NAME(S) AND ADDRESS(ES) Naval Ocean Systems Center San Diego, CA 92152-5000				8. PERFORMING ORGANIZATION REPORT NUMBER TR 1333	
9. SPONSORING/MONITORING AGENCY NAME(S) AND ADDRESS(ES)				10. SPONSORING/MONITORING AGENCY REPORT NUMBER	
11. SUPPLEMENTARY NOTES					
12a. DISTRIBUTION/AVAILABILITY STATEMENT Approved for public release; distribution is unlimited.				12b. DISTRIBUTION CODE	
13. ABSTRACT (Maximum 200 words) This report applies the general theory of canonical eigenvalues, as developed by the authors, to underwater sound propagation in a one-layer bounded duct. For this type of duct, the eigenvalues apply to an entire class of single-layer profiles (slopes may be either negative or positive). Three classes are considered with different upper and lower boundary conditions. They are free-rigid, free-free, and rigid-rigid boundary pairs. Numerical results are given for phase velocity, group velocity, and eigenfunction normalization coefficient, all plotted as functions of frequency.					
14. SUBJECT TERMS underwater acoustics group velocity sound propagation normal mode theory eigenvalues				15. NUMBER OF PAGES 43	
				16. PRICE CODE	
17. SECURITY CLASSIFICATION OF REPORT UNCLASSIFIED	18. SECURITY CLASSIFICATION OF THIS PAGE UNCLASSIFIED	19. SECURITY CLASSIFICATION OF ABSTRACT UNCLASSIFIED	20. LIMITATION OF ABSTRACT SAME AS REPORT		